Computationally efficient high-fidelity plasma simulations by coupling multi-species kinetic and multi-fluid models on decomposed domains

I. A. M. Datta<sup>a</sup>, U. Shumlak<sup>a</sup>

<sup>a</sup> Computational Plasma Dynamics Laboratory, Aerospace and Energetics Research Program, University of Washington, Seattle, WA 98195, United States

#### Abstract

A numerical method is developed for coupling a multi-species kinetic plasma model with a 5Nmoment multi-fluid plasma model. The simulation domain is decomposed such that the local conditions satisfy the corresponding plasma model's region of validity. The method allows for hybrid simulations by formulating each model as a set of conservation laws and using a continuum numerical method to solve each model's governing equations in the subdomains of the decomposed domain. The models are coupled through fluxes across subdomain interfaces. Two methods are explored for the formulation of the fluxes that can be self-consistently represented by both plasma models. One method allows for flux calculations consistent with the 5N-moment multi-fluid plasma model and assumes thermodynamic equilibrium within each species of the kinetic plasma model. The second method ensures conservation of the distribution function as well as mass, momentum, and energy by formulating the fluxes using a composite underlying distribution function at the subdomain interfaces. The methods are compared in 1D1V simulations of a double rarefaction wave and a plasma sheath using the WARPXM framework, which solves each model using the discontinuous Galerkin finite element method. Both methods for formulating the fluxes perform well as the subdomain interface distribution function approaches a Maxwellian, with the consistent method being more robust to larger deviations. A simulation of the magnetized Kelvin-Helmholtz instability in 2D2V is also performed using the consistent method, which demonstrates the potential of the domain-decomposed hybrid method in facilitating speedup and reduction in required computational resources for high-fidelity plasma simulations, allowing for the investigation of problems that are beyond current capabilities.

Keywords: Multi-fluid plasma models, Continuum kinetic plasma models, Hybrid plasma modeling, Discontinuous Galerkin, Plasma sheath, Magnetized Kelvin-Helmholtz instability

## 1. Introduction

The need for high-fidelity computational simulation in the field of plasma physics is widespread, with application in various areas including controlled nuclear fusion [1–4], electric propulsion [5, 6], space physics [7, 8, 9], astrophysics research [10], and active space experiments [11]. Many mathematical models exist to describe the plasma dynamics, with different approximations leading to

Published as Journal of Computational Physics 483, 112073 (2023). doi.org/10.1016/j.jcp.2023.112073 Email addresses: idatta@uw.edu (I. A. M. Datta), shumlak@uw.edu (U. Shumlak)

representations of plasmas at different levels of fidelity. Fluid (or moment) models, which describe plasma dynamics near local thermodynamic equilibrium, comprise one class of mathematical models for numerical simulation. In highly collisional plasmas with Maxwell-Boltzmann (or Maxwellian) probability distribution functions in velocity space, the 5N-moment plasma model, also called the multi-fluid plasma model [12, 13] for N species, effectively describes the plasma dynamics. In plasmas with decreased collisionality, thermalization toward a Maxwellian is less pronounced and the validity of the multi-fluid plasma model decreases. Higher-moment descriptions exist to capture the associated non-Maxwellian dynamics of such plasmas, including the 10N-moment [14] and 13Nmoment [15] models as well as others. With further-reduced collisionalities coupled with magnetic fields driving anisotropies in the distribution function, moment models provide insufficient physical fidelity and lose accuracy. In these situations, kinetic models employing the Boltzmann or Vlasov equations describing the evolution of the distribution function in phase space are needed. In recent years, advances in computational capabilities have made numerical simulation of the Boltzmann and Vlasov equations more tractable [16]; in particular, efficiency has been gained by using continuum techniques similar to those used for moment models, with various treatments under development [17–21]. However, simulations employing the kinetic model are more computationally expensive than those using moment models due to the high-dimensional nature of the Boltzmann and Vlasov equations which are solved in phase space representing physical and velocity dimensions. Physical space can be up to three dimensions, and velocity space can be up to three dimensions, which is denoted 3D3V. In general the kinetic model spans six dimensions in addition to time. The high dimensionality motivates the development of approaches that can accelerate kinetic simulations and reduce the required computational resources without losing the fidelity required to capture the physics of interest. One way to reduce computational cost of kinetic simulations is to decrease the number of degrees of freedom in a phase space mesh in a way that still resolves the relevant physics, such as by using adaptive mesh refinement techniques on the mesh itself [22] or by representing the distribution function spectrally [23]. Another method is to apply a hybrid approach where each species is treated separately, using the kinetic model for one species and a fluid model for another [24–26]. Each species can also be considered individually, such that different models can be used on a particular species in different regions (subdomains) of a simulation domain, which can be determined by comparing the local spatial scales of the plasma, such as the collisional mean free path. This subdomain approach has been studied to various degrees recently, such as by examining a smooth transition region between the models [27, 28], coupling of particle and continuum models [29–39], or coupling between semi-Lagrangian and Eulerian methods for kinetic and fluid models, respectively [40]. Coupling particle and continuum models in particular can be challenging due to statistical scatter present in particle models, which requires a large number of particles to couple to a continuum model at the interface between model subdomains. This issue has been addressed by adopting the particle method to preserve information on a macroscopic scale, which improves coupling with the continuum method while reducing the numerical expense [41].

The methodology of research presented here focuses on the subdomain approach, but uses the same continuum representation and numerical solution method for both the kinetic and fluid models, which eliminates the numerical noise associated with particle models. This approach facilitates accurate coupling between subdomains through specification of the interface conditions between them. Specifically, a discontinuous Galerkin finite element method is used to solve both the multi-fluid plasma model and the multi-species kinetic model on adjacent subdomains, with interface conditions specified through fluxes between the subdomains. Specific attention is applied

to the implementation of these fluxes, expanding on previous work presented in Ref. [42].

This paper is structured as follows. Section 2 describes details of the multi-fluid plasma and multi-species kinetic models. Section 3 reviews the discontinuous Galerkin finite element method for solving the plasma models with a continuum representation. Section 4 presents two kinetic-to-fluid coupling procedures for implementation of the interface conditions between subdomains. Section 5 presents a comparison of the coupling procedures in 1D1V on a double rarefaction wave problem for a single neutral fluid and a plasma sheath problem with ion and electron dynamics. Section 6 presents results using the domain-decomposed hybrid method to simulate the magnetized Kelvin-Helmholtz instability in 2D2V and compares the results to a full kinetic solution. Conclusions are given in Sec. 7.

#### 2. Plasma models

#### 2.1. Multi-species kinetic model

The multi-species kinetic model describes the dynamics of the time-dependent probability distribution function  $f_{\alpha}(\boldsymbol{x}, \boldsymbol{v}, t)$  in phase space composed of physical space and velocity space, where  $\alpha$  represents a particular species of a multi-species plasma. This kinetic model represents the highest physical fidelity that is tractable for studying plasma dynamics. The evolution of the distribution functions in phase space is described by the Boltzmann equation [43], written in non-dimensional form using index notation with the Einstein summation convention as

$$\frac{\partial f_{\alpha}}{\partial t} + v_i \frac{\partial f_{\alpha}}{\partial x_i} + (\omega_c \tau) \frac{Z_{\alpha}}{A_{\alpha}} \left( E_i + \epsilon_{ijk} v_j B_k \right) \frac{\partial f_{\alpha}}{\partial v_i} = \frac{\partial f_{\alpha}}{\partial t} \bigg|_{C}, \tag{1}$$

where the last term represents collisions between particles in the plasma. Equation (1) is coupled to Maxwell's equations in physical space, given by Ampere's law

$$\frac{\partial E_i}{\partial t} - \frac{(\omega_p \tau)^2}{(\omega_c \tau)^2} \epsilon_{ijk} \frac{\partial B_k}{\partial x_j} = -\frac{(\omega_p \tau)^2}{(\omega_c \tau)} \sum_{\alpha} Z_{\alpha} \int v_i f_{\alpha}(\boldsymbol{x}, \boldsymbol{v}, t) d\boldsymbol{v}, \tag{2}$$

and Faraday's law

$$\frac{\partial B_i}{\partial t} + \epsilon_{ijk} \frac{\partial E_k}{\partial x_j} = 0. \tag{3}$$

A simple representation for collisions is given by the Bhatnagar-Gross-Krook (BGK) operator [44], written as

$$\frac{\partial f_{\alpha}}{\partial t} \bigg|_{C} = -\left(\nu_{p}\tau\right)\nu_{\alpha}\left(f_{\alpha} - f_{M_{\alpha}}\right),\tag{4}$$

where  $f_{M_{\alpha}}$  is a Maxwellian distribution function given by

$$f_{M_{\alpha}}(\boldsymbol{v}, n_{\alpha}, \boldsymbol{v}_{\alpha}, T_{\alpha}) = n_{\alpha} \left( \frac{A_{\alpha}}{2\pi T_{\alpha}} \right)^{\frac{d}{2}} \exp\left( \frac{-A_{\alpha}(v_{i} - v_{\alpha_{i}})^{2}}{2T_{\alpha}} \right).$$
 (5)

Here,  $f_{M_{\alpha}}$  is related to  $f_{\alpha}$  through velocity moments

$$n_{\alpha}(\boldsymbol{x},t) = \int f_{\alpha}(\boldsymbol{x},\boldsymbol{v},t) d\boldsymbol{v}, \qquad (6)$$

$$v_{\alpha_i}(\boldsymbol{x},t) = \frac{\int v_i f_{\alpha}(\boldsymbol{x},\boldsymbol{v},t) d\boldsymbol{v}}{n_{\alpha}(\boldsymbol{x},t)},$$
(7)

$$T_{\alpha}(\boldsymbol{x},t) = \frac{\frac{A_{\alpha}}{d} \int \left[v_{i} - v_{\alpha_{i}}(\boldsymbol{x},t)\right]^{2} f_{\alpha}(\boldsymbol{x},\boldsymbol{v},t) d\boldsymbol{v}}{n_{\alpha}(\boldsymbol{x},t)},$$
(8)

where d is the number of velocity-space dimensions. A local spatially-dependent relaxation frequency can be written as shown in Ref. [15] as

$$\nu_{\alpha} = \frac{n_{\alpha}}{A_{\alpha}^{\frac{1}{2}} T_{\alpha}^{\frac{3}{2}}} \ln \Lambda. \tag{9}$$

All equations are normalized by introducing a non-dimensional mass  $A_{\alpha} = m_{\alpha}/m_0$  and non-dimensional charge  $Z_{\alpha} = q_{\alpha}/q_0$ . Normalized reference plasma frequency  $\omega_p \tau = \sqrt{\frac{q_0^2 n_0}{m_0 \epsilon_0}} \tau$ , cyclotron frequency  $\omega_c \tau = \frac{q_0 B_0}{m_0} \tau$ , and collision frequency  $\nu_p \tau \sim \frac{n_0}{m_0^2 T_0^2} \tau$  are introduced, where  $\tau$  is a reference timescale and  $T_0$  is expressed in units of energy. The reference velocity is tied to the thermal speed, which also specifies a reference length scale such that  $v_0 = L/\tau = \sqrt{T_0/m_0}$ . The relation  $B_0^2/\mu_0 = n_0 T_0$  connects  $B_0$  to  $n_0$  and  $T_0$ , which can be used to replace  $\omega_c \tau$  in problems without a magnetic field with  $L/\delta_p$ , where  $\delta_p = c/\omega_p$  is a reference skin depth and c is the speed of light. The normalizing mass is either of protons  $(m_0 = m_p)$  or electrons  $(m_0 = m_e)$  and the normalizing charge is the elementary charge,  $q_0 = e$ . Further details regarding the normalization can be found in Ref. [42].

## 2.2. 5N-moment (multi-fluid) plasma model

The 5N-moment plasma model applies in the limit of high collisionality, where the distribution function approaches a Maxwellian and is derived by taking velocity moments of Eq. (1). Multiplication of Eq. (1) by  $A_{\alpha}$  and integrating over velocity space yields the zeroth velocity moment, which provides the continuity equation

$$\frac{\partial \rho_{\alpha}}{\partial t} + \frac{\partial \left(\rho_{\alpha} v_{\alpha_{i}}\right)}{\partial x_{i}} = 0, \tag{10}$$

where  $\rho_{\alpha} = A_{\alpha} n_{\alpha}$  and  $\mathbf{v}_{\alpha}$  can be obtained using Eqs. (6) and (7). Multiplication of Eq. (1) by  $A_{\alpha}\mathbf{v}$  and integration over velocity space yields the first velocity moment, which provides the momentum equation

$$\frac{\partial \left(\rho_{\alpha} v_{\alpha_{i}}\right)}{\partial t} + \frac{\partial \left(\rho_{\alpha} v_{\alpha_{i}} v_{\alpha_{j}} + p_{\alpha} \delta_{ij}\right)}{\partial x_{j}} = \left(\omega_{c} \tau\right) \frac{Z_{\alpha}}{A_{\alpha}} \rho_{\alpha} \left(E_{i} + \epsilon_{ijk} v_{\alpha_{j}} B_{k}\right), \tag{11}$$

where  $p_{\alpha} = n_{\alpha}T_{\alpha}$  can be obtained using  $\boldsymbol{v}_{\alpha}$  and Eq. (8). Multiplication of Eq. (1) by  $\frac{1}{2}A_{\alpha}(\boldsymbol{v}\cdot\boldsymbol{v})$  and integration over velocity space yields the second contracted moment, providing the energy equation

$$\frac{\partial e_{\alpha}}{\partial t} + \frac{\partial \left[ \left( e_{\alpha} + p_{\alpha} \right) v_{\alpha_i} \right]}{\partial x_i} = \left( \omega_c \tau \right) \frac{Z_{\alpha}}{A_{\alpha}} \rho_{\alpha} v_{\alpha_i} E_i, \tag{12}$$

where  $e_{\alpha} = \frac{p_{\alpha}}{\gamma - 1} + \frac{1}{2}\rho_{\alpha}v_{\alpha}^2$  and  $\gamma$  is the adiabatic index which is related to the number of degrees of freedom,  $D_f$ , through the relationship  $\gamma = (D_f + 2)/D_f$ . Note that this form of the 5N-moment fluid model neglects collisional transport and reactions, and thus describes the dynamics of exact Maxwellian distribution functions. Collisional and reaction terms can be included [45]; however, the focus of this research is to test the coupling between the kinetic model and fluid model without these complications.

# 3. Numerical method for the kinetic and 5N-moment models

The Boltzmann equation as described in Eq. (1) is rewritten in conservative form

$$\frac{\partial f_{\alpha}}{\partial t} + \frac{\partial}{\partial x_{i}} \left( v_{i} f_{\alpha} \right) + \frac{\partial}{\partial v_{i}} \left[ \left( \omega_{c} \tau \right) \frac{Z_{\alpha}}{A_{\alpha}} \left( E_{i} + \epsilon_{ijk} v_{j} B_{k} \right) f_{\alpha} \right] = \frac{\partial f_{\alpha}}{\partial t} \bigg|_{C}. \tag{13}$$

Maxwell's equations, Eqs. (2) and (3), can also be written in conservative form, such that the entire governing system of the kinetic model can be expressed compactly as

$$\frac{\partial q_i}{\partial t} + \frac{\partial \mathcal{F}_{ij}}{\partial x_j} = \mathcal{S}_i, \tag{14}$$

where q is the solution vector for the equation set,  $\mathcal{F}$  is the flux tensor, and  $\mathcal{S}$  represents source terms. The x coordinate is generalized to represent spatial position x and velocity v in Eq. (13). The 5N-moment model written in Eqs. (10), (11), and (12) with Maxwell's equations can also be expressed as in Eq. (14).

Expressing the governing equation system in the form of Eq. (14) facilitates solution with the discontinuous Galerkin finite element method using the WARPXM (Washington Approximate Riemann Plasma) framework [13]. The framework provides algorithms that solve plasma physics problems on unstructured grids using fluid and kinetic models. The unified framework also simplifies hybridization, allowing for interfacing between different models being solved in different subdomains of a simulation. The coupling of the Boltzmann equation in Eq. (13) as well as the fluid equations in Eqs. (10), (11), and (12) to Maxwell's equations in Eqs. (2) and (3) also allows for global solutions to Maxwell's equations over the entire domain, which can aid hybridization, as has been shown for coupling of codes using a global electrostatic Poisson equation solver [46].

The discontinuous Galerkin method in WARPXM involves subdividing the simulation domain into discrete elements and projecting the conserved variables,  $q_i$  in Eq. (14), onto a set of basis functions  $\phi_m$  of order m such that the numerical approximation is represented as

$$q_i = q_{im}\phi_m. (15)$$

Equation (14) is then multiplied by each basis function and integrated over each element volume  $\Omega$ , yielding the weak form integral equation for each basis function

$$\int_{\Omega} \frac{\partial q_i}{\partial t} \phi_m dV + \oint_{\partial \Omega} \mathcal{F}_{ij} n_j \phi_m dS - \int_{\Omega} \mathcal{F}_{ij} \frac{\partial \phi_m}{\partial x_j} dV = \int_{\Omega} \mathcal{S}_i \phi_m dV, \tag{16}$$

where the divergence theorem has been applied to the flux tensor term. The mesh consists of simplex elements such as lines, triangles, or tetrahedrons in physical space and rectilinear hypercubes (lines, rectangles, rectangular prisms) in velocity space. Phase-space elements for the kinetic

model are constructed using tensor products of the physical-space and velocity-space elements. The integration of the surface integral over an element surface  $\partial\Omega$  in Eq. (16) is computed using a summation of surface integrals over each element face,

$$\oint_{\partial\Omega} \mathcal{F}_{ij} n_j \phi_m dS = \sum_{\gamma}^{\Gamma} \int_{\partial\Omega^{\gamma}} \left( \mathcal{F}_{ij} n_j \right)_{\gamma}^* \phi_m dS, \tag{17}$$

where  $\gamma$  represents a particular face with normal n and  $\Gamma$  is the total number of faces for the element. The asterisk on the term in the integrand denotes that the flux is single-valued at each location along the surface  $\partial\Omega$ .

The time integration of Eq. (16) is accomplished using an explicit Runge-Kutta (ERK) timestepping method. The combination of spatial and temporal discretizations produces a compact, high-order scheme with an optimal convergence rate of  $\mathcal{O}(h^{N+1})$  for element size h and polynomial basis order N [47]. Lagrange interpolating polynomials based on Legendre-Gauss-Lobatto quadrature node locations are used for the basis functions, yielding a nodal scheme in which the coefficients in Eq. (15) correspond to solution values at the node locations.

The discontinuous Galerkin method allows discontinuous solutions at element faces, leading to Riemann problems that must be solved in order to construct the appropriate fluxes given by the  $(\mathcal{F}_{ij}n_j)^*_{\gamma}$  terms in the surface integrals of Eq. (17). The solutions to the Riemann problems, whether exact or approximate [12, 48–50], are the numerical fluxes.

Further details of the discontinuous Galerkin method used in the WARPXM framework can be found in Refs. [51, 52]. Details of the ERK time-stepping algorithm to advance Eq. (16) are described in Ref. [42].

The WARPXM framework has been used to simulate plasmas using the 5N-moment and kinetic models. Examples of simulations involving the 5N-moment model include those of Z-pinch dynamics [53], drift turbulence in field reversed configurations [13, 54], and magnetic reconnection [51]. Examples of simulations involving the kinetic model include those of Landau damping and the two-stream instability [42] as well as the Dory-Guest-Harris instability [55].

The domain-decomposed hybrid method for coupling the 5N-moment and kinetic models is implemented through the formulation of the numerical flux at the subdomain interfaces. Thus, an overview of the numerical fluxes used for each model is given in Sec. 3.1, while the determination of the numerical fluxes between the models at subdomain interfaces is detailed in Sec. 4.

## 3.1. Numerical fluxes at element faces for plasma models

The numerical flux is often expressed in the local frame of an element face, so it is convenient to first rewrite the flux in terms of rotation operators, such that

$$(\mathcal{F}_{ij}n_j)^*_{\gamma} = (R^{\gamma})^{-1}\,\tilde{\mathcal{F}}(R^{\gamma}q_i) \equiv (R^{\gamma})^{-1}\,\tilde{\mathcal{F}}(\tilde{q}_i^{\gamma}),\tag{18}$$

where  $R^{\gamma}$  rotates from a global grid frame to a local frame along the face  $\gamma$  where the normal points outward from the element in the surface integral,  $(R^{\gamma})^{-1}$  rotates back from the local frame to the global frame, and  $\tilde{\mathcal{F}}(\tilde{q}_i^{\gamma})$  is the normal flux vector in the local frame [56].  $\tilde{\mathcal{F}}(\tilde{q}_i^{\gamma})$  can then be calculated using a flux splitting method given by

$$\tilde{\mathcal{F}}(\tilde{q}_i^{\gamma}) = \frac{1}{2} \left( \tilde{\mathcal{F}}(\tilde{q}_i^{\gamma-}) + \tilde{\mathcal{F}}(\tilde{q}_i^{\gamma+}) \right) + \frac{1}{2} \left| \tilde{A} \right|_{ij} \left( \tilde{q}_j^{\gamma-} - \tilde{q}_j^{\gamma+} \right), \tag{19}$$

where – refers to values of  $\tilde{q}_i^{\gamma}$  on the internal element  $\Omega$  and + refers to values of  $\tilde{q}_i^{\gamma}$  on the external element adjacent to element  $\Omega$  at the face  $\gamma$  for the surface integral in Eq. (17). The tensor  $\left|\tilde{A}\right|_{ij}$  is a diagonalized approximation of the flux Jacobian  $\partial \tilde{\mathcal{F}}(\tilde{q}_i)/\partial \tilde{q}_j$  using the absolute values of its eigenvalues [57]. For Eq. (13), which behaves as a multi-dimensional advection equation, the flux Jacobian approximation is for the scalar distribution function and does not require rotation and is exact, such that

$$\left(\mathcal{F}_{ij}n_{j}\right)_{\gamma}^{*} = \tilde{\mathcal{F}}\left(f_{i}^{\gamma}\right) = \frac{\tilde{a}}{2}\left(f^{\gamma-} + f^{\gamma+}\right) + \frac{1}{2}\left|\tilde{a}\right|\left(f^{\gamma-} - f^{\gamma+}\right),\tag{20}$$

where  $\tilde{a}$  is either the local velocity on spatial flux faces or the acceleration on velocity flux faces projected onto the frame of the face normal. The Maxwell system is linear and yields an exact flux Jacobian, resulting in

$$\tilde{\mathcal{F}}(\tilde{E}_{i}^{\gamma}) = \frac{1}{2} \frac{(\omega_{p}\tau)}{(\omega_{c}\tau)} \begin{bmatrix} 0 \\ \frac{(\omega_{p}\tau)}{(\omega_{c}\tau)} \left(\tilde{B}_{z}^{\gamma-} + \tilde{B}_{z}^{\gamma+}\right) + \left(\tilde{E}_{y}^{\gamma-} - \tilde{E}_{y}^{\gamma+}\right) \\ -\frac{(\omega_{p}\tau)}{(\omega_{c}\tau)} \left(\tilde{B}_{y}^{\gamma-} + \tilde{B}_{y}^{\gamma+}\right) + \left(\tilde{E}_{z}^{\gamma-} - \tilde{E}_{z}^{\gamma+}\right) \end{bmatrix}, \tag{21a}$$

$$\tilde{\mathcal{F}}(\tilde{B}_{i}^{\gamma}) = \frac{1}{2} \begin{bmatrix} 0 \\ -\left(\tilde{E}_{z}^{\gamma-} + \tilde{E}_{z}^{\gamma+}\right) + \frac{(\omega_{p}\tau)}{(\omega_{c}\tau)} \left(\tilde{B}_{y}^{\gamma-} - \tilde{B}_{y}^{\gamma+}\right) \\ \left(\tilde{E}_{y}^{\gamma-} + \tilde{E}_{y}^{\gamma+}\right) + \frac{(\omega_{p}\tau)}{(\omega_{c}\tau)} \left(\tilde{B}_{z}^{\gamma-} - \tilde{B}_{z}^{\gamma+}\right) \end{bmatrix},$$
(21b)

written in vector form corresponding to Eqs. (2) and (3) respectively. The fluid system is nonlinear and thus finding  $\left|\tilde{A}\right|_{ij}$  is more complicated. However, numerous approximate solutions known as approximate Riemann solvers exist [12, 52]. A few that have been implemented for the 5*N*-moment model are Rusanov [58], HLL [59], and Roe [60] methods.

#### 4. Domain-decomposed hybrid method implementation using numerical fluxes

180

The domain-decomposed hybrid method applies the multi-fluid plasma model and multi-species kinetic model on adjacent subdomains of a simulation. At subdomain interfaces the distribution function solutions for each model can be different, as illustrated in Fig. 1, where  $f_F$  refers to the Maxwellian distribution function constructed from fluid variable solutions to the multi-fluid plasma model using Eq. (5) and  $f_K$  refers to the distribution function solution to the multi-species kinetic model. Interface conditions determine the interaction between the multi-fluid plasma model and multi-species kinetic model at the subdomain interfaces, which can be specified through the surface numerical flux as described in Sec. 3.1. Two approaches are considered to define the numerical fluxes at the subdomain interfaces.

The first approach defines the numerical flux in a manner that is consistent with the assumptions associated with each model, e.g. the distribution functions used to calculate the numerical flux for the multi-fluid plasma model are Maxwellian. The method achieves the consistency for the multi-fluid plasma model by extracting variables from  $f_K$  that define a Maxwellian distribution function with the same first three velocity moments as  $f_K$  to enable the flux splitting given by Eq. (19). The numerical flux for the multi-species kinetic model is calculated from  $f_F$  and  $f_K$ 

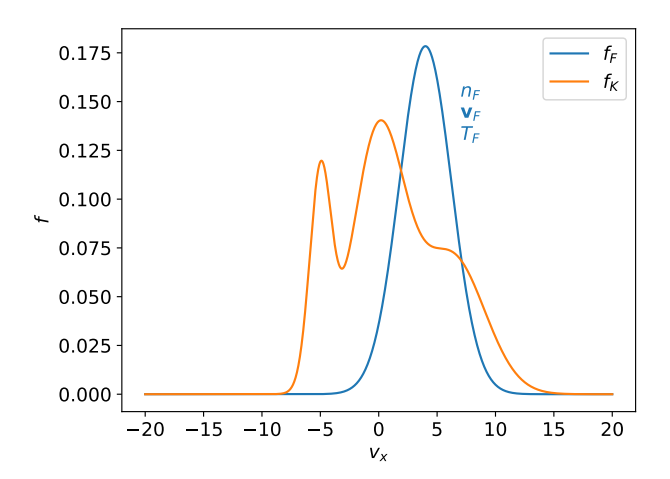


Figure 1: Illustrative distribution functions at a subdomain interface between the multi-fluid plasma model,  $f_F$ , and the multi-species kinetic model,  $f_K$ . The fluid distribution function is a Maxwellian calculated using Eq. (5) from the fluid variables  $n_F$ ,  $v_F$ , and  $T_F$ , which are the solutions to the multi-fluid plasma model at the subdomain interface. Solutions for only a single species are shown for illustration, but solutions for multiple species can also exist. The differences between  $f_F$  and  $f_K$  are also exaggerated for illustrative purposes. In practice,  $f_F$  and  $f_K$  will have only small differences.

using Eq. (20), which does not assume any particular distribution function profile. Details of the consistent method, referred to as the direct variable translation method, are described in Sec. 4.1.

The second approach defines the numerical flux for the two plasma models based on an underlying composite distribution function, which ensures the conservation of mass, momentum, and energy. Details of the conservative method, referred to as the composite distribution function method, are given in Sec. 4.2. In the limit where  $f_K$  approaches a Maxwellian distribution function identical to  $f_F$ , both approaches provide consistency and conservation.

# 4.1. Direct variable translation method

The direct variable translation method calculates the numerical flux for the multi-fluid plasma model and multi-species kinetic model in a manner that is consistent with the assumptions of the multi-fluid plasma model, which is that the distribution functions on either side of the subdomain interface are Maxwellians. Figure 2 illustrates the method for a particular species.

The procedure to calculate the numerical flux for the multi-fluid plasma model is to translate  $f_K$  at the subdomain interface into fluid variables  $n_K$ ,  $v_K$ , and  $T_K$  using Eqs. (6), (7), and (8). These fluid variables are then combined with fluid variable solutions from the multi-fluid plasma model at the subdomain interface,  $n_F$ ,  $v_F$ , and  $T_F$ , using Eq. (19) to calculate a numerical flux. The effect is that the numerical flux for the multi-fluid plasma model is calculated from Maxwellian distribution functions  $f_F$  and  $f_{K_M}$  as shown in Fig. 2, where  $f_{K_M}$  is a Maxwellian distribution function with the same first three velocity moments as  $f_K$ . In this manner, the numerical flux for the multi-fluid plasma model is consistent with the assumption of Maxwellian distribution functions required for the fluid approximation.

The calculation of the numerical flux for the multi-species kinetic model is performed after the translation of  $n_F$ ,  $v_F$ , and  $T_F$  to  $f_F$ , allowing for application of Eq. (20) using  $f_F$  and  $f_K$ . No assumptions need to be made in the numerical flux calculations for the multi-species kinetic model, which does not impose any restriction on distribution function shape.

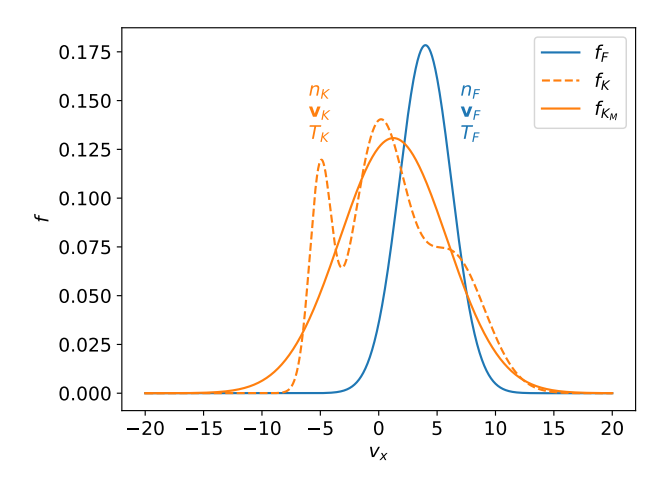


Figure 2: Illustrative distribution functions at a subdomain interface between the multi-fluid plasma model,  $f_F$ , and the multi-species kinetic model,  $f_K$  as in Fig. 1. Velocity moments of  $f_K$  are calculated using Eqs. (6), (7), and (8) yielding fluid variables  $n_K$ ,  $v_K$ , and  $T_K$  that describe an equivalent Maxwellian distribution function according to Eq. (5), denoted as  $f_{K_M}$ . The direct variable translation method calculates the numerical flux for the multi-fluid plasma model by approximating  $f_K$  as  $f_{K_M}$  and applying flux splitting in Eq. (19) on the fluid variables  $(n_F, v_F, T_F, n_K, v_K, T_K)$ . In this way the method consistently calculates the fluid numerical flux. The numerical flux for the multi-species kinetic model is calculated by using  $f_F$  and  $f_K$  in Eq. (20). As with Fig. 1, a single species is shown, however, the same procedure can be performed for multiple species. The differences between  $f_F$  and  $f_K$  are also exaggerated for illustrative purposes. In practice,  $f_F$  and  $f_K$  will have only small differences.

While the direct variable translation method provides consistency in that the numerical flux for the multi-fluid plasma model is calculated assuming Maxwellian distribution functions, deviation of  $f_K$  from a Maxwellian causes loss in accuracy, due to inexact representation of the distribution function using only the velocity moments that yield  $n_K$ ,  $v_K$ , and  $T_K$ . This loss in accuracy manifests in a loss of conservation of the distribution function as well as the fluid model conserved variables of mass, momentum, and energy due to numerical fluxes being calculated for the multifluid plasma and multi-species kinetic models based on different distribution functions ( $f_F$  and  $f_{K_M}$  for the fluid model as opposed to  $f_F$  and  $f_K$  for the kinetic model). Conservation is provided, however, as  $f_K$  approaches a Maxwellian identical to  $f_F$  at the subdomain interface.

#### 4.2. Composite distribution function method

230

While the direct variable translation method provides consistency in the specification of the numerical flux for the multi-fluid plasma model and becomes conservative as  $f_K$  approaches  $f_F$ , the composite distribution function method provides conservation for arbitrary  $f_K$  and becomes consistent as  $f_K$  approaches  $f_F$ . This conservative approach is performed by constructing a composite distribution function,  $f_C$ , from  $f_F$  and  $f_K$ , from which the numerical fluxes for the multi-fluid plasma model and multi-species kinetic model are calculated directly.

The method for constructing  $f_C$  is illustrated in Fig. 3 for the case of a subdomain interface in a local frame of reference in which the multi-fluid plasma model is solved on the left and the multi-species kinetic model is solved on the right. The numerical flux for the kinetic model as given in Eq. (20) shows that for  $v_x \geq 0$ ,  $\mathcal{F} = v_x f_F$  and for  $v_x < 0$ ,  $\mathcal{F} = v_x f_K$ , where the tildes are dropped for clarity of notation. This flux can be obtained from a composite distribution function

defined as

$$f_C(f_K, f_F) = \begin{cases} f_K & \text{if } v_x < 0\\ f_F & \text{if } v_x \ge 0, \end{cases}$$
 (22)

as illustrated in Fig. 3. If the multi-species fluid model is solved on the right of the subdomain interface and the kinetic model is solved on the left, the definition of  $f_C$  would be reversed, given by

$$f_C(f_F, f_K) = \begin{cases} f_F & \text{if } v_x < 0\\ f_K & \text{if } v_x \ge 0. \end{cases}$$
 (23)

The numerical flux for each model can then be calculated from this composite distribution function. For the multi-species kinetic model, application Eq. (20) on  $f_F$  and  $f_K$  yields the numerical flux, identical to the calculation for the direct variable translation method, and by inspection of Eqs. (22) and (23), is equivalent to  $\mathcal{F} = v_x f_C$ .

The numerical fluxes for the multi-fluid plasma model are calculated from the velocity moments of  $f_C$  that yield the flux tensor terms in Eqs. (10), (11), and (12). The flux tensor terms for a particular species, written for an element face  $\gamma$  at a subdomain interface between models with normal n, are given by

$$\left(\mathcal{F}_{i(\rho_{\alpha})}n_{i}\right)_{\gamma}^{*} = \left(\rho_{\alpha}v_{\alpha i}n_{i}\right)_{\gamma}^{*} = n_{i\gamma}\int v_{i}\left(A_{\alpha}f_{C,\alpha}\right)d\boldsymbol{v},\tag{24}$$

$$\left(\mathcal{F}_{ij(\rho_{\alpha}\boldsymbol{v}_{\alpha})}n_{j}\right)_{\gamma}^{*} = \left(\left[\rho_{\alpha}v_{\alpha i}v_{\alpha j} + p_{\alpha}\delta_{ij}\right]n_{j}\right)_{\gamma}^{*} = n_{j\gamma}\int v_{j}\left(A_{\alpha}v_{i}f_{C,\alpha}\right)d\boldsymbol{v},\tag{25}$$

$$\left(\mathcal{F}_{i(e_{\alpha})}n_{i}\right)_{\gamma}^{*} = \left(\left[\left(e_{\alpha} + p_{\alpha}\right)v_{\alpha i}\right]n_{i}\right)_{\gamma}^{*} = n_{i\gamma} \int v_{i}\left(\frac{1}{2}A_{\alpha}v_{j}v_{j}f_{C,\alpha}\right)d\boldsymbol{v},\tag{26}$$

for Eqs. (10), (11), and (12), respectively.

Deriving a flux from the same composite distribution function for each plasma model ensures conservation of the distribution function and the conserved variables in the fluid model, mass, momentum, and energy. However, for arbitrary  $f_K$  far from  $f_F$ , the fluid fluxes calculated in Eqs. (24), (25), and (26) are not solutions based on consistent assumptions of Maxwellian distribution functions, as would be the case if applying Eq. (19) using fluid variables. The composite distribution function method can lead to inaccurate solutions when  $f_K$  is far from  $f_F$ . As with the direct variable translation method though, conservation and consistency are recovered as  $f_K$  approaches  $f_F$ .

In the next section, solutions using the direct variable translation and the composite distribution function methods are compared for some illustrative cases coupling the multi-fluid plasma model in 1D to the multi-species kinetic model in 1D1V. Performance is compared through observation of the solutions as well as measurements of conservation properties. A metric measuring the deviation from a Maxwellian distribution function in the kinetic subdomains, given by

$$\chi_{\alpha} = \frac{\int |f_{\alpha} - f_{M_{\alpha}}| \, d\mathbf{v}}{n_{\alpha}},\tag{27}$$

where  $f_{M_{\alpha}}$  is a Maxwellian distribution function related to  $f_{\alpha}$  through the fluid variables in Eqs. (6), (7), and (8) [17, 19], is also used to compare the direct variable translation and composite distribution function methods.

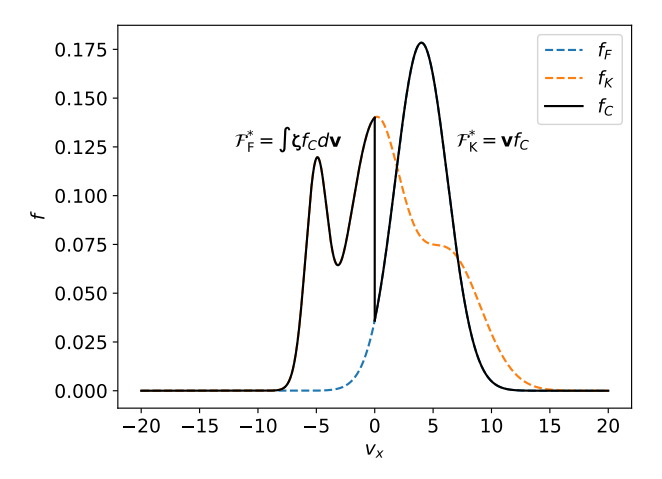


Figure 3: Illustration of a composite distribution function,  $f_C$  constructed from  $f_F$  and  $f_K$  at a subdomain interface between the multi-fluid plasma model and multi-species kinetic model, as shown in Fig. 1, for the case of the multi-fluid plasma model solved to the left of the interface and the multi-species kinetic model solved to the right. The composite distribution function is constructed by considering the portions of  $f_K$  and  $f_F$  that advect across the subdomain interface, which by inspection of Eq. (20) yields  $f_C$  defined by Eq. (22). For the composite distribution function method, the numerical flux for the multi-species kinetic model is calculated from  $f_K$  and  $f_F$  using Eq. (20) or equivalently as  $vf_C$ , which is identical to the direct variable translation method. The numerical flux using the composite distribution function method for the multi-fluid plasma model is then constructed from velocity moments of  $f_C$ , given by  $\mathcal{F}_{\zeta}^* = \int \zeta f_C dv$  for  $\zeta = [A_{\alpha}v, A_{\alpha}vv, \frac{1}{2}A_{\alpha}vv^2]$ . This leads to a conservative method in which the numerical fluxes for the multi-fluid plasma model and multi-species kinetic model are constructed from the same underlying composite distribution function. The composite distribution function is shown for a single species, but as with the direct variable translation method, the composite distribution function method can be performed for multiple species. The differences between  $f_F$  and  $f_K$  are also exaggerated for illustrative purposes. In practice,  $f_F$  and  $f_K$  will have only small differences.

# 5. Domain-decomposed hybrid simulations using the direct variable translation method and the composite distribution function method in 1D1V

The direct variable translation and composite distribution function methods described in Sec. 4 are used to couple the multi-fluid plasma model described in Sec. 2.2 to the multi-species kinetic model described in Sec. 2.1. The domain-decomposed hybrid method is applied to 1D test problems – a neutral gas wave propagation and a two-fluid plasma sheath formation. For the rest of this paper, the multi-fluid plasma model will be denoted as the fluid model and the multi-species kinetic model will be denoted as the kinetic model.

## 5.1. Neutral gas test of the hybrid coupling approaches for a double rarefaction wave problem

A double rarefaction wave problem [61–63] involving a single thermalized neutral fluid is used to test the direct variable translation and composite distribution function methods in the limit where Maxwellian distribution functions exist on either side of a subdomain interface. The problem couples the fluid model in 1D with the kinetic model in 1D1V and was previously studied in Ref. [42] to test the direct variable translation method.

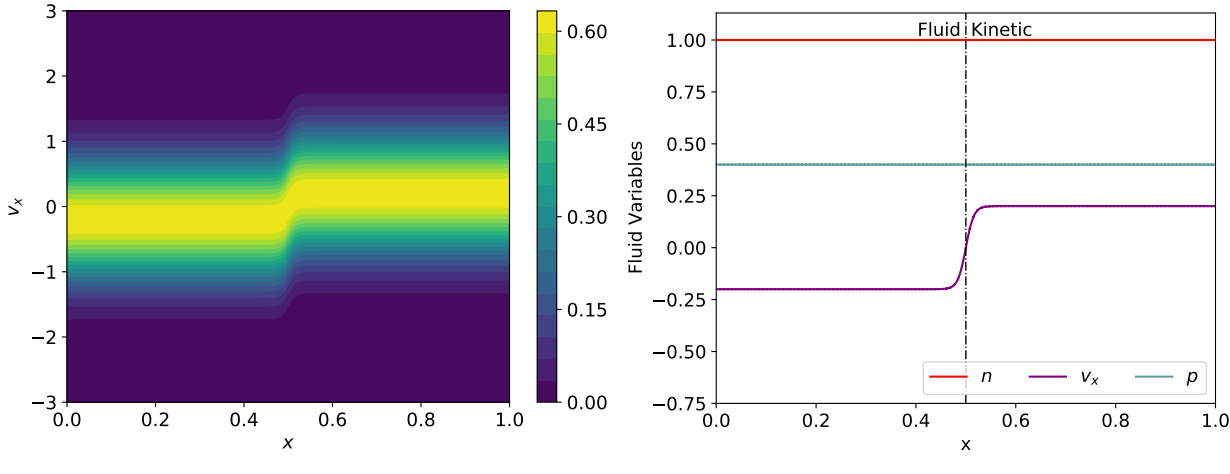
The initial condition consists of a uniform density and pressure, with  $\rho = 1.0$  and p = 0.4 over a physical space domain given by  $x \in [0,1]$ . The velocity is initialized to produce rarefaction waves propagating outward from  $x = x_c = 0.5$  by setting a positive velocity in the right portion of the domain,  $v_{x_R} = 0.2$ , and a negative velocity in the left portion of the domain,  $v_{x_L} = -0.2$ . The velocity smoothly transitions at  $x = x_c$  using the form

$$v_x = \frac{v_{x_L}}{2} \left[ 1 - \tanh \left\{ \frac{2\pi \left( x - x_c \right)}{d} \right\} \right] + \frac{v_{x_R}}{2} \left[ 1 + \tanh \left\{ \frac{2\pi \left( x - x_c \right)}{d} \right\} \right], \tag{28}$$

where d = 0.1 is a measure of the transition width. The smooth transition ensures adequate resolution of the gradient, enabling accurate grid convergence studies.

Simulations are performed with the domain decomposed into left and right subdomains separated at  $x = x_c$ . For  $x < x_c$ , the fluid model is solved and for  $x > x_c$ , the kinetic model is solved. Both models use a single species with mass A = 1. The species is also charge neutral with Z = 0, eliminating electromagnetic source terms in Eqs. (11) and (12) as well as the velocity-direction flux in Eq. (13), which also removes the need to solve Maxwell's equations, Eqs. (2), and (3). Simulations are performed using the direct variable translation method for coupling of the fluid model with the kinetic model. The simulations are then repeated using the composite distribution function method. In the subdomain where the kinetic model is solved, the initial condition is set by using the initialized density and pressure and velocity according to Eq. (28) to define corresponding Maxwellian distribution functions using Eq. (5). The initial conditions for the distribution function and fluid variables are plotted in Fig. 4.

For consistency with the single spatial degree of freedom in a 1D1V kinetic simulation, the adiabatic index is set to  $\gamma=3$  in the fluid subdomain. The simulations are performed to t=0.15 with the velocity-space domain of the kinetic model defined by  $v_x \in [-10,10]$ . Second-order polynomial elements are used, comprising of 128 line elements in x, while the velocity-space resolution is varied to yield phase-space elements for resolutions of  $N_x \times N_{v_x}$ :  $128 \times 20$ ,  $128 \times 40$ ,  $128 \times 80$ ,  $128 \times 160$ ,  $128 \times 320$ , and  $128 \times 640$ . A third-order ERK method is used for timestepping and Rusanov numerical fluxes are used in the solution for the fluid model. A simulation is also performed using the fluid model in both the left and right subdomains, denoted in the rest of this



- (a) Distribution function for  $x \in [0, 1]$  and  $v_x \in [-3, 3]$ . The velocity space for the simulations however spans  $v_x \in [-10, 10]$ .
- (b) Fluid variables for  $x \in [0, 1]$ .

Figure 4: Initial condition for the double rarefaction wave simulation on a grid of  $128 \times 640$  second-order polynomial elements. Figure 4a shows the initial condition for the distribution function and Fig. 4b shows corresponding fluid variables n,  $v_x$ , and p.

section as the fluid simulation. Simulations at all velocity-space resolutions are also performed using the kinetic model in both subdomains, denoted as the kinetic simulations.

Collisions drive the kinetic distribution function towards a Maxwellian according to Boltzmann's H-theorem [43], which is required for validity of the fluid model, so a collision operator of the form in Eq. (4) is included where the kinetic model is solved. The relaxation parameter for the collision operator is set using  $\nu_p \tau = 1$  and varying  $\nu$  until thermalization is achieved.

Figure 5 shows fluid variables, calculated using moments of the distribution function in the kinetic subdomains and as solutions to the fluid model in the fluid subdomains, for all simulations with  $\nu$  values of 10, 100 and 1000 for the  $128 \times 640$  resolution case at t=0.15. Agreement between the kinetic model using the collision operator and the fluid model is found with increasing  $\nu$ . The solutions using the direct variable translation and composite distribution function methods also generally agree well with the fluid and kinetic simulation solutions. However, the level of agreement reduces between the location of the initial jump in velocity at  $x_c$  and the rarefaction wave as it moves in time for low collision frequencies. This can be seen more clearly in a closeup of the number density as shown in Fig. 6. For lower collision frequencies, the discrepancy increases at  $x_c$ , corresponding to the initial velocity jump and the subdomain interface between the fluid and kinetic solutions, which causes a mismatch in the solution using either hybrid method, and is generally larger for the composite distribution function method. This mismatch is diminished for both coupling methods with increasing collision frequency, allowing the fluid moments calculated from the kinetic solution to approach a Maxwellian distribution function that matches the fluid solution.

Figure 5d visually confirms the matching distribution function at the subdomain interface for the  $\nu = 1000$  case. As described in Sec. 4, the direct variable translation and composite distribution function methods are conservative and consistent when this subdomain interface distribution function is Maxwellian. Measurements of  $\chi$  as defined in Eq. (27) confirm that the distribution function

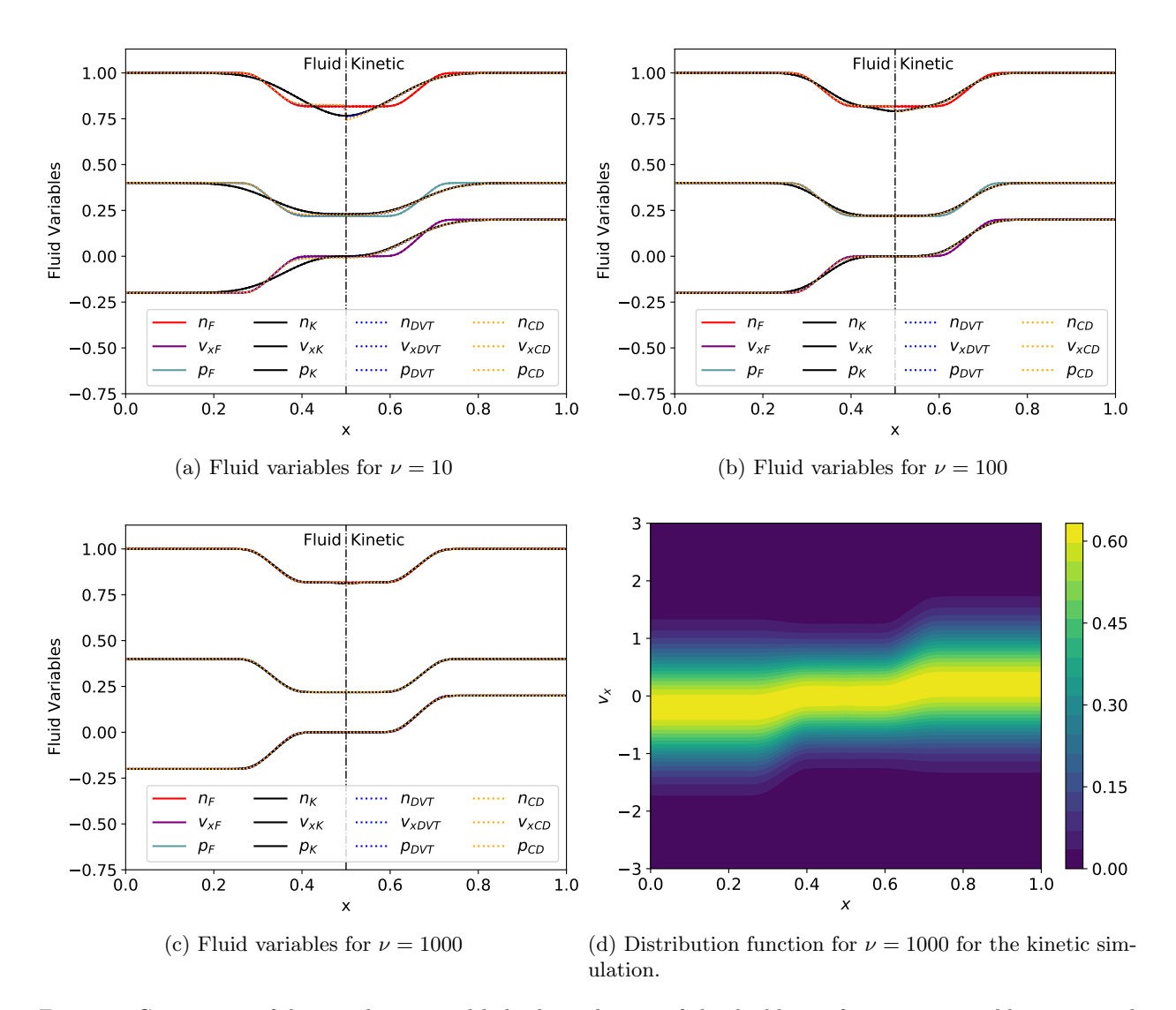


Figure 5: Comparison of domain-decomposed hybrid simulations of the double rarefaction wave problem a on grid of  $128 \times 640$  second-order polynomial elements at t=0.15. Fluid variables, measured by taking moments of the distribution function in the kinetic subdomain, and as solutions to the fluid model in the fluid subdomain, are shown in Figs. 5a, 5b, and 5c for  $\nu=10$ , 100, and 1000. F, K, DVT, and CD denote fluid, kinetic, hybrid using the direct variable translation method, and hybrid using the composite distribution function method simulations, respectively. The distribution function for the  $\nu=1000$  case is shown in Fig. 5d for the kinetic simulation. The BGK operator with increasing  $\nu$  relaxes distribution functions towards Maxwellians on subdomains where the kinetic model is solved, allowing for coupling of the fluid and kinetic models using the direct variable translation and composite distribution function methods at the subdomain interface at  $x=x_c=0.5$  with minimal error.

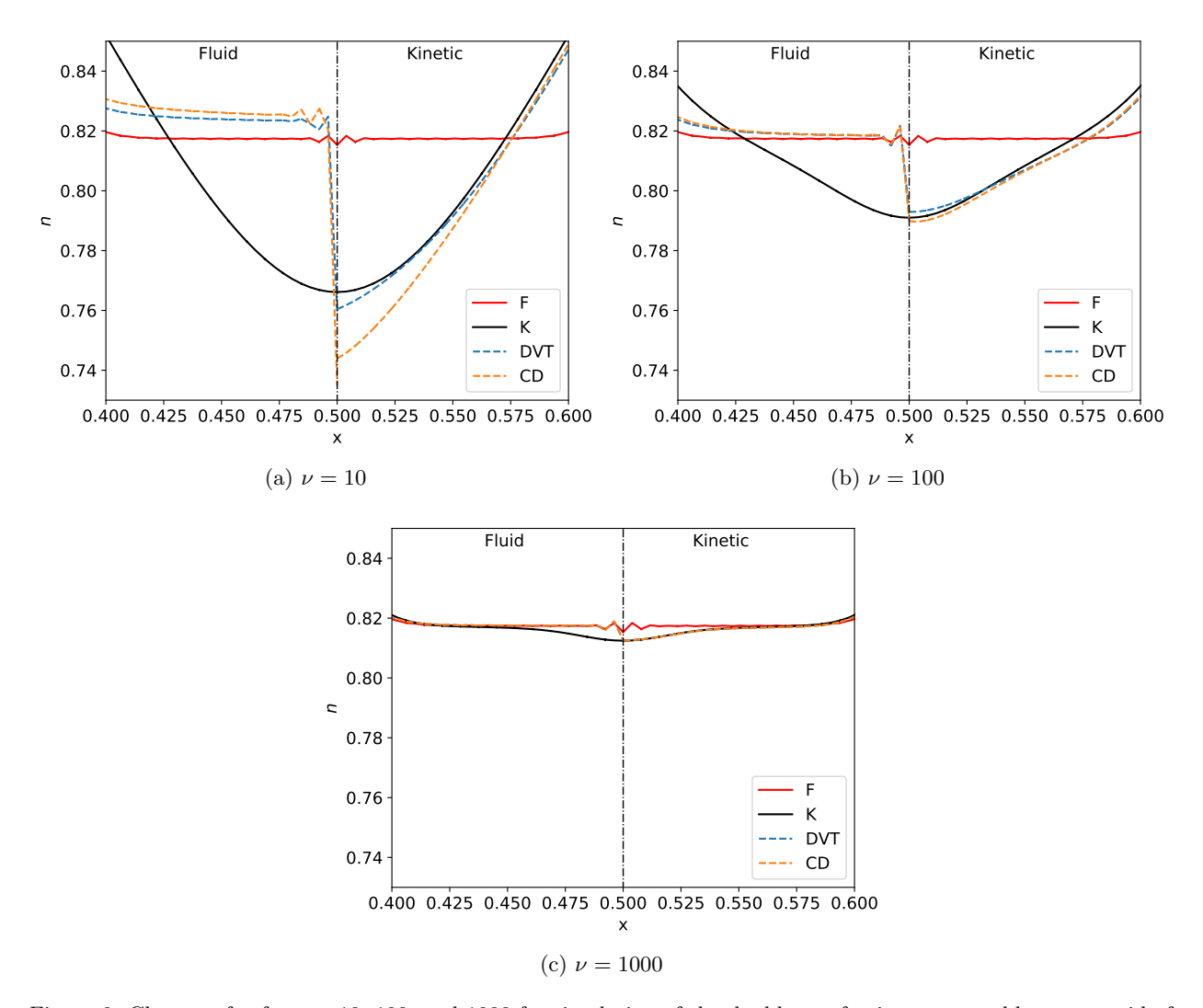


Figure 6: Closeup of n for  $\nu=10$ , 100, and 1000 for simulation of the double rarefaction wave problem on a grid of  $128\times640$  second-order polynomial elements at t=0.15. With increasing  $\nu$ , the fluid and kinetic solutions approach each other, allowing for better matching of the solution in each subdomain using the direct variable translation and composite distribution function methods. Note the DVT and CD lines closely follow each other in Fig. 6c for  $\nu=1000$ .

does approach a Maxwellian with increased collision frequency, as seen in Fig. 7, which plots  $\chi$  for  $\nu=10,\,100,\,$  and 1000 for the  $128\times640$  resolution simulations. Figure 7 shows that the subdomain interface distribution function approaches a Maxwellian (lower values of  $\chi$ ) for increasing collision frequency. Figure 7 also shows that  $\chi$  measured in the hybrid simulations using the direct variable translation and composite distribution function methods closely matches  $\chi$  measured in the kinetic simulation for the higher collision frequencies, further indicating similar evolution of the solution using the kinetic and fluid models when the distribution function approaches a Maxwellian.

A further check of the coupling performance of the direct variable translation and composite distribution function methods can be made by measuring mass, momentum, and energy conservation. As described in Sec. 4, the composite distribution function method should provide better conservation properties than the direct variable translation method in general, but both should provide conservation when the distribution functions on either side of the subomain interface approach the same Maxwellian. A norm is defined to measure the conservation properties, given by

350

$$L_2^{q_i} = \sqrt{\sum_{t=0}^{0.15} \left( \int_0^1 q_i(t) dx + \left[ \left( \mathcal{F}_{ij(q_i(t))} n_j \right)_{x=0} + \left( \mathcal{F}_{ij(q_i(t))} n_j \right)_{x=1} \right] \Delta t - \int_0^1 q_i(t=0) dx \right)^2}, \quad (29)$$

where  $q_i = [\rho, p_x, e]$  are the conserved variables in the one-dimensional fluid model in Eqs. (10), (11), and (12), where for x-momentum,  $p_x \equiv \rho v_x$ . Equation (29) is the  $L_2$ -norm of the difference in the integral of  $q_i$  over the physical-space domain at various times compared with t = 0, calculated at intervals of  $\Delta t = 0.0015$ . To account for outflow of mass, momentum, and energy at domain boundaries, the time-integrated flux of  $q_i$  is included in the  $\mathcal{F}_{ij}(q_i(t))n_j$  terms, calculated using Eqs. (24), (25), and (26), where  $n_j$  is the unit normal pointing out of the simulation domain. Assuming the distribution functions are Maxwellian and constant at the domain boundaries (the double rarefaction wave does not reach the boundaries at t = 0.15), these fluxes can be calculated from the initial condition density, velocity, and pressure as

$$\left(\mathcal{F}_{(\rho)}n_x\right)_{x=0} + \left(\mathcal{F}_{(\rho)}n_x\right)_{x=1} = 0.2 + 0.2 = 0.4$$
 (30)

$$\left(\mathcal{F}_{(p_x)}n_x\right)_{x=0} + \left(\mathcal{F}_{(p_x)}n_x\right)_{x=1} = -0.44 + 0.44 = 0 \tag{31}$$

$$\left(\mathcal{F}_{(e)}n_x\right)_{x=0} + \left(\mathcal{F}_{(e)}n_x\right)_{x=1} = 0.124 + 0.124 = 0.248$$
 (32)

Equation (29) is calculated for the various velocity-space resolutions and plotted in Fig. 8 for  $\nu=1000$ . Values of  $L_2$  for mass, momentum, and energy converge to floors once velocity space is adequately resolved when  $1/\Delta v_x=4$ , corresponding to the  $128\times80$  resolution simulation. The converged  $L_2$  values for the simulations using the composite distribution function method are similar to those for the kinetic simulations. This confirms the conservation property of the composite distribution function method. The conservation of mass, momentum, and energy using the direct variable translation method is reduced compared to the kinetic simulations and those using the composite distribution function method, indicated by the higher converged values reached in Fig. 8. Similar behavior is observed at lower collision frequencies, but with higher converged values of  $L_2$  for mass, momentum, and energy for each hybrid method. This trend can be seen in Table 1, which shows the  $L_2$  values for  $\nu=10$ , 100, and 1000 for the simulations at the  $128\times640$  resolution. This indicates that even the direct variable translation method does conserve

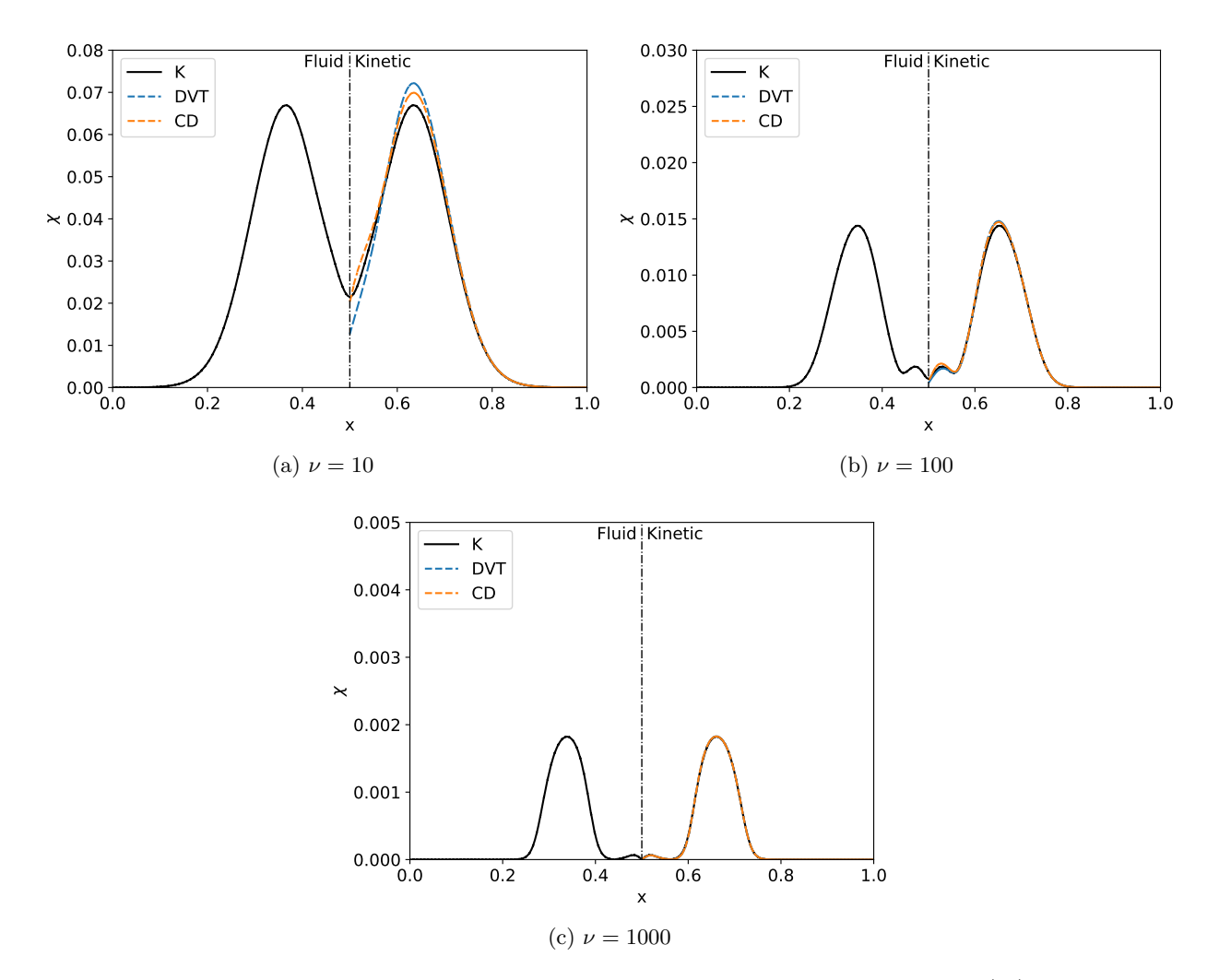


Figure 7: Deviation from a Maxwellian distribution function is indicated by  $\chi$ , defined in Eq. (27), for the double rarefaction simulations at t=0.15, measured for a kinetic simulation using  $128\times640$  second-order polynomial elements in phase space for  $\nu=10,\,100,\,$  and 1000. Values of  $\chi$  are also plotted on the right subdomain for simulations using the direct variable translation and composite distribution function methods at the same resolution. Values of  $\chi$  reduce in simulations with higher  $\nu$ , indicating distribution functions that are closer to Maxwellian. Higher  $\nu$  also allows for better matching of  $\chi$  for simulations employing either hybrid method to the kinetic simulation. Note the DVT and CD lines closely follow each other in Fig. 7c for  $\nu=1000.$  Also note that  $\chi$  is only plotted on the left subdomain for the kinetic simulation, as it is 0 by definition in the fluid model.

	$\nu$	F	K	DVT	CD
$L_2^{\rho}$	10	$2 \times 10^{-13}$	$1 \times 10^{-8}$	$8 \times 10^{-4}$	$7 \times 10^{-9}$
	100	$2\times10^{-13}$	$5\times10^{-13}$	$5 \times 10^{-5}$	$3 \times 10^{-13}$
	1000	$2\times 10^{-13}$	$7\times10^{-13}$	$1 \times 10^{-5}$	$3\times10^{-13}$
$L_2^{p_x}$	10	$3 \times 10^{-16}$	$2 \times 10^{-16}$	$1 \times 10^{-3}$	$2 \times 10^{-8}$
_	100	$3 \times 10^{-16}$	$4 \times 10^{-15}$	$2 \times 10^{-4}$	$7 \times 10^{-13}$
	1000	$3 \times 10^{-16}$	$1\times10^{-13}$	$2 \times 10^{-6}$	$5 \times 10^{-14}$
$L_2^e$	10	$5 \times 10^{-14}$	$8 \times 10^{-8}$	$2 \times 10^{-3}$	$4 \times 10^{-8}$
	100	$5 \times 10^{-14}$	$2\times10^{-12}$	$4 \times 10^{-4}$	$8 \times 10^{-13}$
	1000	$5\times 10^{-14}$	$1 \times 10^{-13}$	$9\times10^{-6}$	$6\times10^{-14}$

Table 1: The norm  $L_2^q$  as defined in Eq. (29) for the double rarefaction wave problem plotted for the  $128 \times 640$  resolution case using second-order polynomial elements for  $\nu = 10$ , 100, and 1000. Mass, momentum, and energy are conserved to a higher degree for the composite distribution function method compared with the direct variable translation method, with both exhibiting better conservation as the distribution functions are more closely approximated as Maxwellians with increasing collision frequency.

mass, momentum, and energy to a higher degree as the subdomain interface distribution function approaches a Maxwellian, as postulated in Sec. 4.

Overall, the double rarefaction wave test indicates good performance using the direct variable translation and composite distribution function methods for coupling between the fluid and kinetic models for a single neutral fluid approaching a Maxwellian. The coupling is performed with minimal error or instability with good conservation properties in the Maxwellian limit.

# 5.2. Multi-species plasma test of the hybrid coupling approaches for a plasma sheath

385

The performance of the coupling methods described in Sec. 4 can be further assessed through application to a realistic problem involving multiple charged species in the presence of electromagnetic fields and where kinetic effects are essential to the dynamics. The 1D plasma sheath development provides such an assessment. As with the double rarefaction wave problem, the plasma sheath was studied in Ref. [42] using the direct variable translation method, and is expanded upon to include the composite distribution function method for comparison.

The plasma sheath development is simulated on a one-dimensional domain bounded by grounded electrodes (or walls), as described in Ref. [64]. The normalization used is as described in Ref. [42], and is restated for convenience, with reference values of density  $n_0 = 10^{19}$  m<sup>-3</sup>, temperature  $T_0 = 1$  eV, and Debye length scale  $L = \sqrt{\frac{\epsilon_0 T_0}{n_0 q_0^2}} = 2.35 \ \mu\text{m}$ . A normalizing proton mass  $m_0 = m_p$  is set, leading to  $\omega_p \tau = 1$  and  $L/\delta_p = v_0/c = 3.265 \times 10^{-5}$  using the normalization described in Sec. 2.1. A realistic mass ratio is used such that  $A_i = 1$  and  $A_e = 1/1836$  while the charges are  $Z_i = 1$  and  $Z_e = -1$ . Ions and electrons are simulated with initial conditions of  $n_i = n_e = 1$ ,  $v_{x_i} = v_{x_e} = 0$ , and  $T_i = T_e = 10$  on a 1D1V grid where the physical space is defined by a grid of  $x \in [-128, 128]$  where for hybrid simulations, for  $x \in [-128, -96]$  and  $x \in [96, 128]$ , the kinetic model is solved and for  $x \in [-96, 96]$ , the fluid model is solved. The velocity space spans  $v_{\alpha} = [-6v_{\text{th}_{\alpha}}, 6v_{\text{th}_{\alpha}}]$  for each species  $\alpha$  where  $v_{\text{th}_{\alpha}} = \sqrt{T_{\alpha}/A_{\alpha}}$ . A simulation using the kinetic model for both ions and electrons over all subdomains is also performed, denoted the kinetic simulation for the rest of this section. Boundary conditions are outflow for the distribution functions in phase space and conducting walls for the fields. Second-order polynomial spatial and velocity elements are used, with  $\Delta x = 1$  and  $\Delta v_{x_{\alpha}} = v_{\text{th}_{\alpha}}/4$ , along with third-order ERK timestepping.

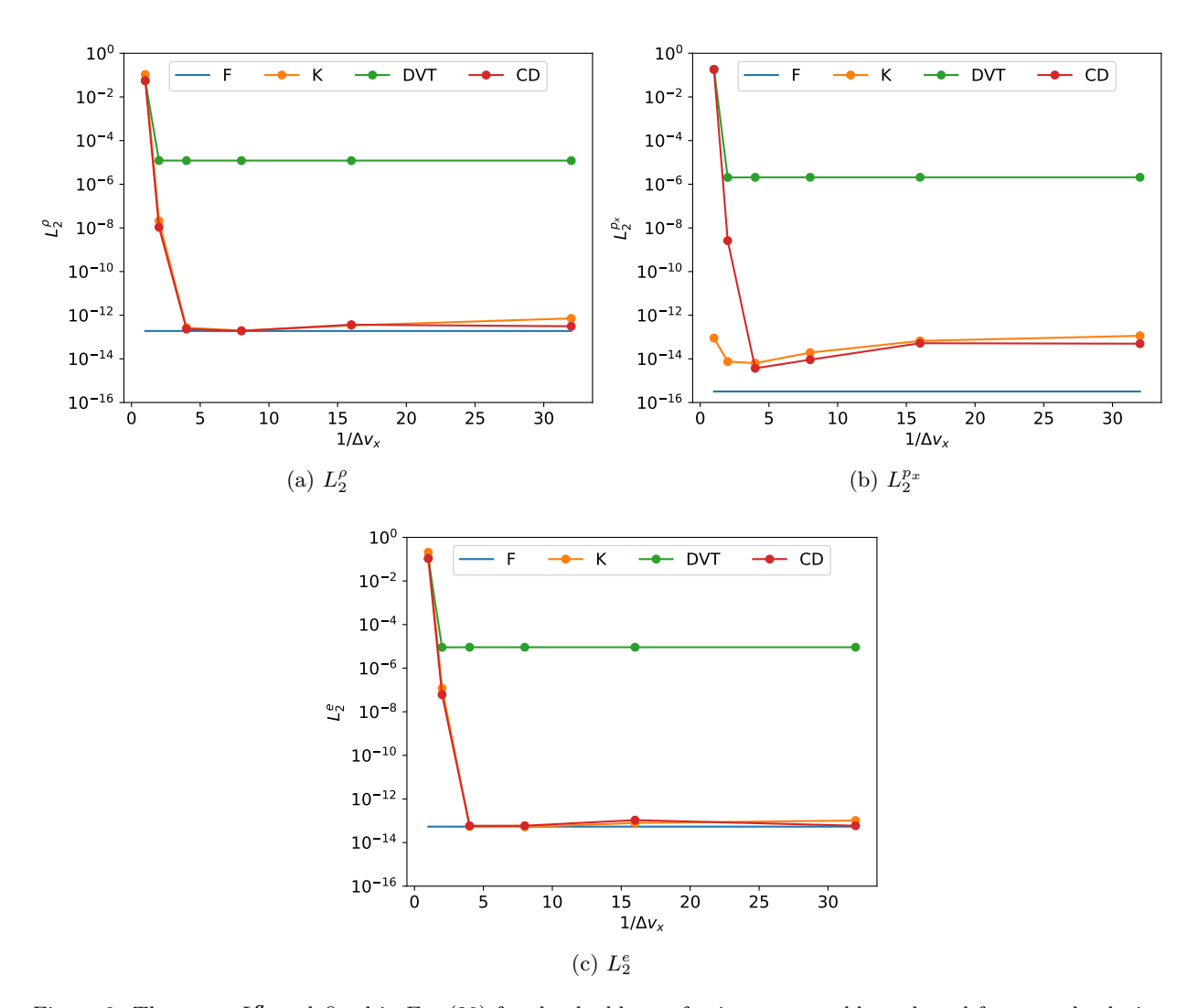


Figure 8: The norm  $L_2^q$  as defined in Eq. (29) for the double rarefaction wave problem plotted for several velocity-space resolutions using second-order polynomial elements in the velocity direction for  $\nu=1000$ . All models use 128 second-order polynomial spatial elements. The values of  $L_2^q$  reach converged values as the velocity space is accurately resolved when  $1/\Delta v_x=4$ , corresponding to the  $128\times80$  resolution case. Mass, momentum, and energy are conserved to a higher degree for the composite distribution function method compared with the direct variable translation method.

The simulations are run to  $t\omega_{pe} = 20$ , where  $\omega_{pe} = \sqrt{Z_e^2 n_e/A_e}$  is the non-dimensional electron plasma frequency. As with the 1D1V double rarefaction wave problem, the adiabatic index is set to  $\gamma = 3$  in the fluid subdomain. For the fluid model, Roe fluxes are employed for the solution to Eq. (19) [12, 60].

Due to the mass ratio and equivalent initial ion and electron temperatures, the electron dynamics are much faster than for ions. As the highest-velocity electrons leave the domain and become absorbed by the walls, a positive potential forms and the electron distribution function loses symmetry and no longer remains Maxwellian. This happens immediately adjacent to the walls and emphasizes the utility of the domain-decomposed hybrid method, which allows for the kinetic solution in the subdomains adjacent to the walls and the fluid solution away from them. A BGK collision operator as written in Eq. (4) with locally-dependent collision frequency as given in Eq. (9) is thus added to the simulations in the kinetic subdomains for the electrons, with  $\nu_p \tau = 1$  and  $\ln \Lambda = 10$ . This collision frequency is highest away from the walls where the fluid model becomes valid, and decreases as the plasma enters the sheath region [64] where the distribution function is expected to be far from Maxwellian. As discussed in Sec. 2, collisions between ions and electrons are neglected. Also, the simulations presented in this section do not replenish the high-energy electrons and ions absorbed by the walls to achieve steady-state. The focus of the simulations is to compare behavior using the kinetic model over the entire domain with the hybrid approach using the direct variable translation and composite distribution function methods early enough in time before significant loss of electron and ion density occur. Simulations involving steady-state sheaths obeying the Bohm criterion by replenishing electrons and ions can be performed in future work. One way to do so would be to add an ionization source term for each species from a background distribution of neutrals [64, 65].

Figure 9 shows the ion and electron distribution functions at  $t\omega_{pe} = 20$  for the kinetic simulation as well as simulations employing the direct variable translation and composite distribution function hybrid methods. For the hybrid simulations, Maxwellian distribution functions constructed from the solutions to the fluid model in the middle subdomain are shown. Figures 9d and 9f indicate an accumulation of the electron distribution function at the subdomain interfaces for the simulations using the hybrid methods, which is more pronounced for the composite distribution function method. No such accumulation appears to occur in the ions, however.

Figures 10 and 11 show comparisons of the fluid variables n,  $v_x$ , p, and T for ions and electrons, respectively, for each of the simulations as well as  $\chi$  defined in Eq. (27). Figure 10 shows agreement in the ion solution, which is expected due to the low value of  $\chi$  at the subdomain interfaces, as illustrated in Fig. 10e, as well as the smooth transition at the subdomain interfaces in Figs. 9c and 9e. The jumps in electron density, pressure, and temperature seen in Figs. 11a, 11c, and 11d however confirm the observed accumulation of the distribution functions in Figs. 9d and 9f. The electron density and temperature discontinuities are more pronounced, however, for the composite distribution function method compared with the direct variable translation method. Figures 11b and 11c also show smoother electron velocity and pressure transitions between subdomains for the composite distribution function method compared with the direct variable translation method. Additionally, both hybrid methods increase the amplitude of oscillations in the fluid subdomain for the electrons, as shown in Figs. 11a, 11b, 11c, and 11d.

Figure 11e shows a value of  $\chi_e$  of about 0.03 at the subdomain interfaces for the kinetic simulation at  $t\omega_{pe} = 20$ . The discontinuities and oscillations present in the simulations using the direct variable translation and composite distribution function methods indicate that at this value

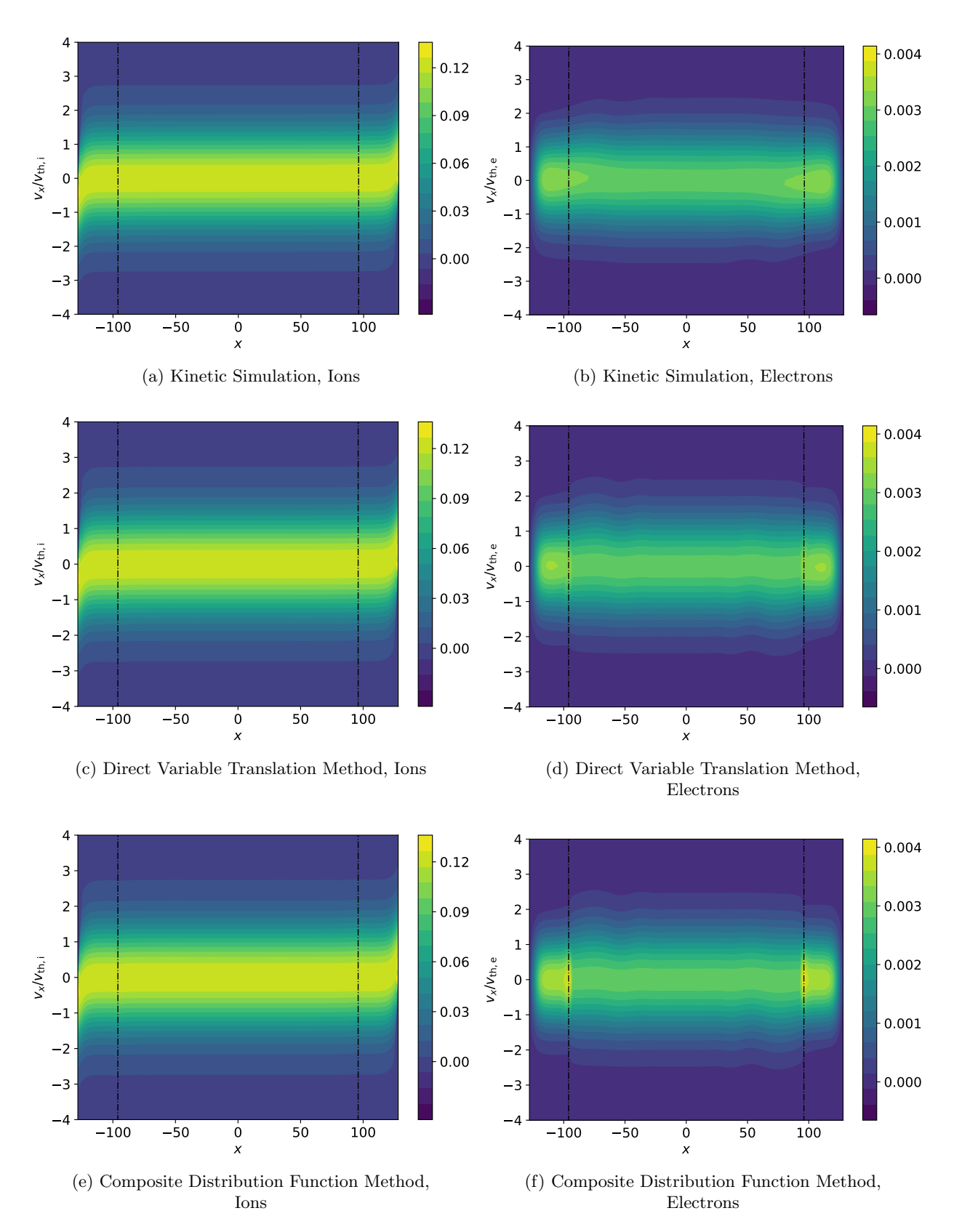


Figure 9: Ion and electron distribution functions for a two-species plasma sheath at  $t\omega_{pe}=20$ . The kinetic simulation results are shown as well as results for the hybrid simulations using the direct variable translation and composite distribution function methods. For the hybrid simulations, the fluid model is solved on the middle subdomain for  $x \in [-96, 96]$  and the kinetic model is solved on the side subdomains for  $x \in [-128, -96]$  and  $x \in [96, 128]$ . Second-order elements are used in physical space with  $\Delta x=1$  and second-order elements are used in velocity space for  $v_x \in [-6v_{\text{th}_{i,e}}, 6v_{\text{th}_{i,e}}]$  with  $\Delta v_{x_{\text{i,e}}} = v_{\text{th}_{i,e}}/4$ . Maxwell's equations are solved on all subdomains in physical space. Maxwellian distribution functions computed from fluid variables are shown in the middle subdomain where the fluid model is solved in the hybrid simulations. An accumulation of the electron distribution function at the subdomain interfaces at  $x_{si} = \pm 96$  is seen in the hybrid simulations, which is more pronounced for the composite distribution function method. The ion distribution functions in the hybrid simulations are indistinguishable from those in the kinetic simulation.

of  $\chi_e$  the fluid model is not valid for the electron species at the subdomain interfaces, and thus application of the fluid model at these locations produces inaccurate results. The further decrease in  $\chi_e$  towards the center of the domain, as seen in Fig. 11e, indicates an advantage in moving the subdomain interface toward the center of the domain.

Simulations are thus performed using the direct variable translation and composite distribution function methods with the subdomain interface at  $x_{si}=\pm 64$ , which reduces the size of the fluid subdomain while increasing the size of the kinetic subdomains. Plots of fluid variables and  $\chi_{\rm e}$  for these simulations including the kinetic simulation are shown in Fig. 12. The density and temperature jumps when using the direct variable translation and composite distribution function methods are found to be reduced compared to when the subdomain interfaces are closer to the walls. The hybrid simulation results more closely follow the kinetic simulation results when the kinetic subdomains adjacent to the walls are expanded. The lower value of  $\chi_{\rm e}$  of about 0.01 seen in Fig. 12e at the  $x_{si}=\pm 64$  subdomain interface, 1/3 of the value of 0.03 seen in Fig. 11e for  $x_{si}=\pm 96$  with better agreement between the kinetic and hybrid simulations, confirms that more accurate solutions are found as the distribution function at subdomain interfaces approaches a Maxwellian.

A measure of the electron mass and energy integrated over the domain of the hybrid simulations compared to the kinetic simulation for both cases of the subdomain interface location are shown in Fig. 13. This compares the conservation properties for each hybrid method against the kinetic simulation. The mass and energy are computed according to

465

$$\frac{\Delta M}{M_K} = \left| \frac{\int \rho(t)dx - \int \rho_K(t)dx}{\int \rho_K(t)dx} \right|,\tag{33}$$

$$\frac{\Delta E}{E_K} = \left| \frac{\int e(t)dx - \int e_K(t)dx}{\int e_K(t)dx} \right|,\tag{34}$$

where K refers to the kinetic simulation quantity. Integrated momentum is maintained at zero for all hybrid and kinetic simulations. As described in Sec. 4 and seen for the double rarefaction wave problem in Sec. 5.1, the composite distribution function method achieves mass and energy conservation that is closer to the kinetic simulation than by using the direct variable translation method. Moving the subdomain interface away from the wall where  $\chi_e$  is reduced, however, improves mass and energy conservation and solution accuracy for both hybrid methods. The improvements further support the observations in Figs. 11 and 12, which show the solutions using both hybrid methods that are closer to the kinetic simulation when the kinetic subdomains are expanded.

To counteract the numerical oscillations and accumulation of the distribution function at a particular subdomain interface due to either the direct variable translation or composite distribution function method, it may also be useful to monitor and remove any charge imbalance at the subdomain interface, calculated using Gauss' Law,

$$\Delta \rho_c \equiv \rho_c - \frac{(L/\delta_p)}{(\omega_p \tau)^2} \frac{\partial E_i}{\partial x_i},\tag{35}$$

where  $\rho_c = Z_i \left( n_{i_f} + n_{i_k} \right) + Z_e \left( n_{e_f} + n_{e_k} \right)$  is the local charge density from fluid and kinetic ions and electrons at the subdomain interface. To remove the charge imbalance, enough density could be added to one of the species, for example to the fluid electrons to zero  $\Delta \rho_c$  in Eq. (35). However,

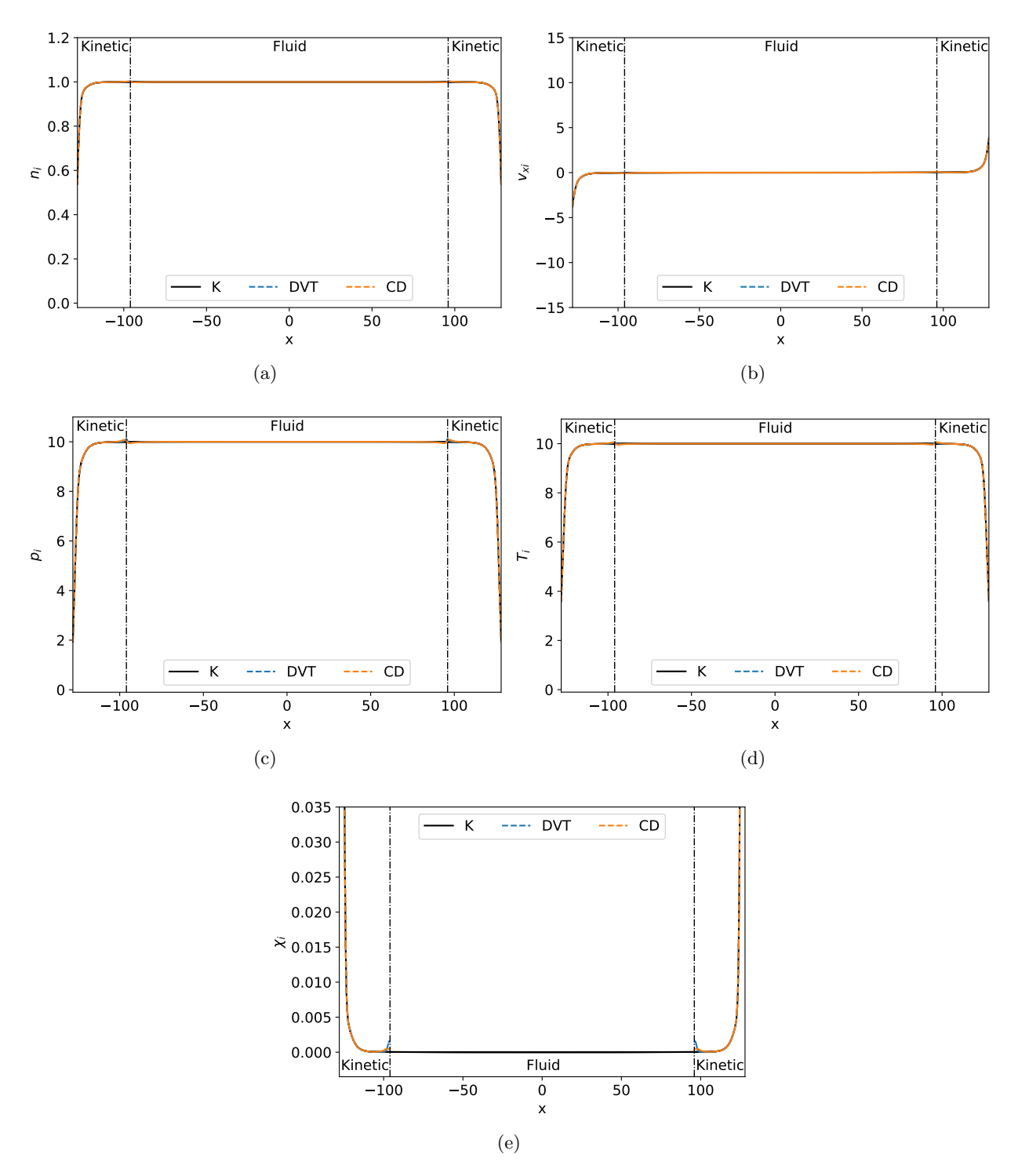


Figure 10: Ion fluid variables  $n, v_x, p$ , and T and the  $\chi$  metric for Maxwellian deviation for the two-species plasma sheath at  $t\omega_{pe}=20$ . Simulations involving the kinetic model solved over all subdomains as well as the direct variable translation and composite distribution function methods are plotted. The subdomain interfaces at  $x_{si}=\pm 96$  are shown. No large jumps or oscillations of ion fluid variables occur at the subdomain interfaces for the hybrid simulations.

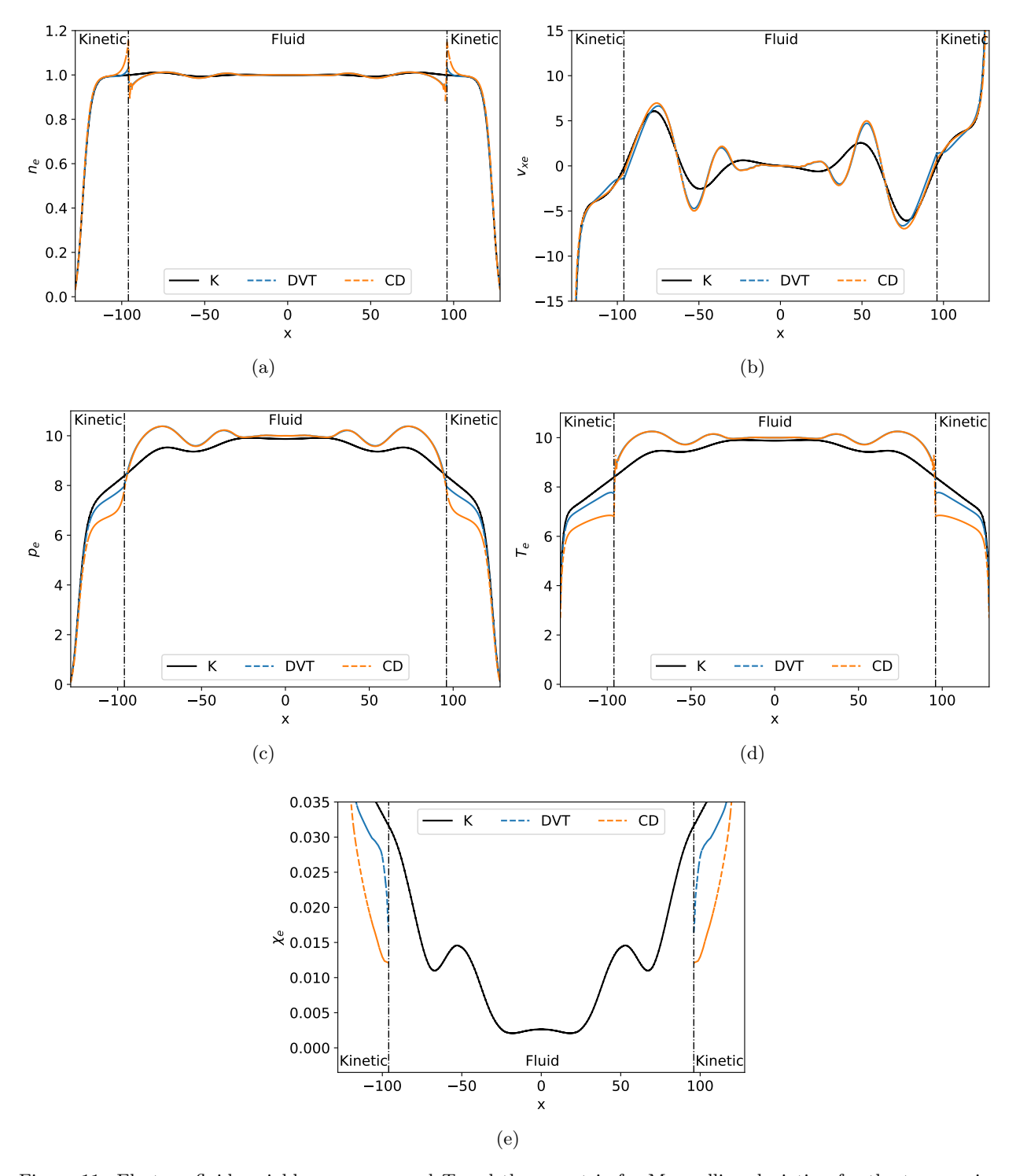


Figure 11: Electron fluid variables  $n, v_x, p$ , and T and the  $\chi$  metric for Maxwellian deviation for the two-species plasma sheath at  $t\omega_{pe}=20$ . Simulations involving the kinetic model solved over all subdomains as well as the direct variable translation and composite distribution function methods are plotted. The subdomain interfaces at  $x_{si}=\pm96$  are shown. The simulation using the composite distribution function method exhibits larger jumps in electron density and temperature at the subdomain interfaces than the simulation using the direct variable translation method. Both hybrid methods also produce increased amplitudes of oscillations in the fluid subdomain compared to the kinetic simulation.

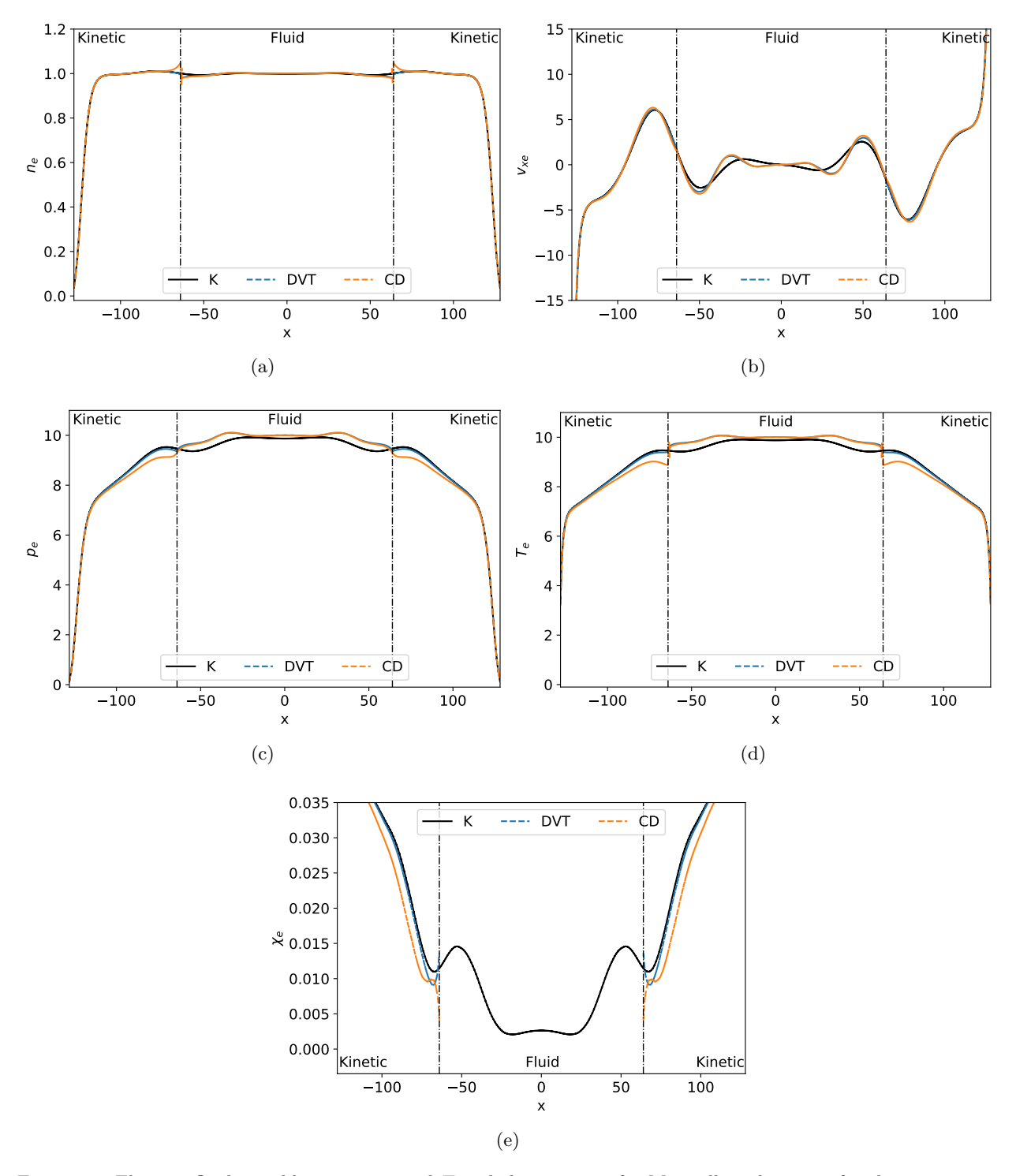


Figure 12: Electron fluid variables  $n, v_x, p$ , and T and the  $\chi$  metric for Maxwellian deviation for the two-species plasma sheath at  $t\omega_{pe}=20$ , as described in Fig. 11, but with larger kinetic subdomains, with the subdomain interfaces at  $x_{si}=\pm 64$ . Compared with the case of the subdomain interface at  $x_{si}=\pm 96$ , the jumps in electron density, pressure, and temperature are reduced for the case of the subdomain interface further from the wall at  $x_{si}=\pm 64$  where the electron distribution function is closer to Maxwellian. The amplitude of the oscillations in the fluid subdomain is reduced with the expanded kinetic subdomains.

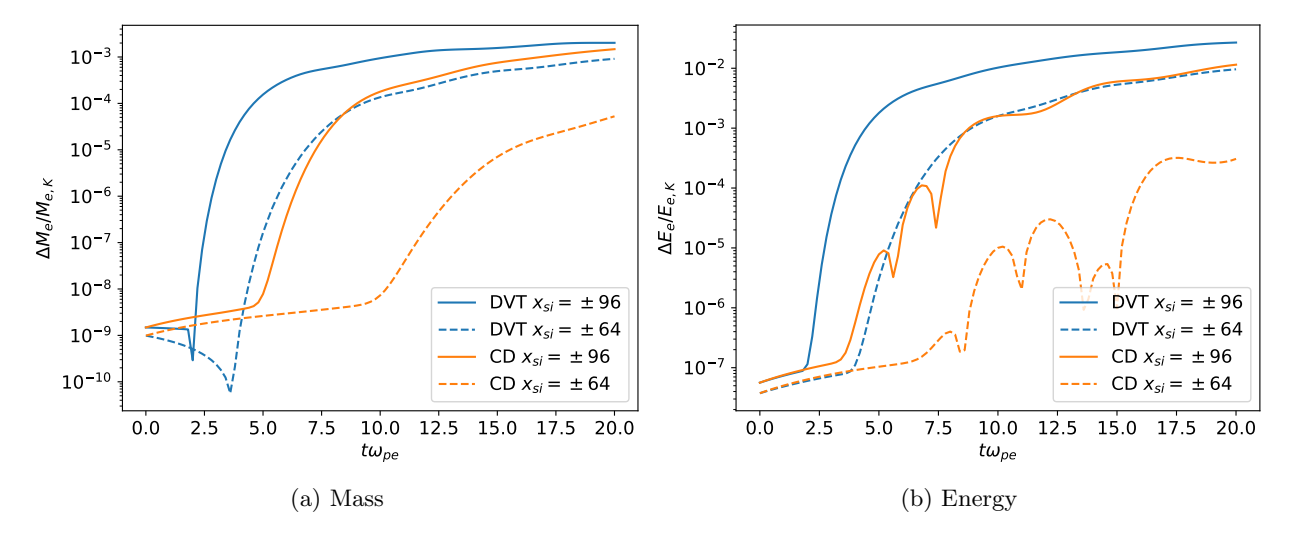


Figure 13: Integrated mass and energy for the two-species plasma sheath problem relative to the kinetic simulation for the hybrid simulations using the direct variable translation and composite distribution function methods. The cases with subdomain interfaces at  $x_{si} = \pm 96$  and  $x_{si} = \pm 64$  are compared. The conservation properties are better for the composite distribution function method than for the variable translation method. However, a larger improvement is achieved by placing the subdomain interface at a location where the fluid model is valid.

this can cause a lack of global conservation in density. A Lagrange multiplier formulation could be used to enforce the charge conservation while minimizing the amount of added mass. This approach can be examined in future work, though as has been shown using Figs. 11, 12, and 13, placing the subdomain interface where the fluid model is valid reduces inaccuracies and the loss of conservation properties.

## 5.3. Conclusions from one dimensional hybrid method tests

Simulations involving the double rarefaction wave in Sec. 5.1 and plasma sheath in Sec. 5.2 show that both the direct variable translation and composite distribution function methods for model coupling between the multi-fluid plasma model and the multi-species kinetic model are viable when the distribution function at the subdomain interface is close to Maxwellian. The plasma sheath simulations show that the direct variable translation method is more robust than the composite distribution function method, with smaller jumps in the fluid variables at the subdomain interfaces. Conservation properties are significantly improved by placing the subdomain interfaces where  $\chi$  is small, which validates the fluid model. The improved conservation properties are observed for both the composite distribution function method and the direct variable translation method.

Further work in one dimension could be done to characterize the effect of either hybrid method for model coupling as the subdomain interface is moved. One test can be performed by initializing a distribution function with a bump-on-tail [66] on one side of the spatial domain that transitions to a Maxwellian on the other side. The placement of the subdomain interface between the fluid model and the kinetic model for hybrid simulations using the direct variable translation or composite distribution function methods could be studied for its impact on the solution. This would allow for an understanding of the range of values of  $\chi$  that permit solutions with minimal jumps in fluid variables and loss of conservation properties. It would also allow for other possible metrics

for non-fluid behavior to be tested as a way to determine the efficacy of the subdomain interface placement. Such analysis could be the topic of future research.

The next section will use the direct variable translation method to simulate the magnetized Kelvin-Helmholtz instability problem in 2D2V, demonstrating the effectiveness of the method for reducing computational costs while maintaining physical accuracy.

# 6. Domain-decomposed hybrid simulations of the magnetized Kelvin-Helmholtz instability in 2D2V

The direct variable translation hybrid method is now applied in 2D2V to the magnetized Kelvin-Helmholtz instability. This instability is driven by velocity shear and governs the transport of collisionless low-beta plasmas perpendicular to a background magnetic field. Previous work systematically studied the magnetized Kelvin-Helmholtz instability through derivation of linear growth rates using the Hall MHD model as well as simulations using higher-fidelity models including the multi-fluid plasma model as described in Sec. 2.2 and a multi-species kinetic model using a Vlasov-Poisson formulation for electrostatics [17]. The multi-fluid plasma model captures the physics of charge separation and diamagnetic drift (not captured by single-fluid MHD) in the shear layer of the magnetized Kelvin-Helmholtz instability while the kinetic model additionally resolves effects associated with finite Larmor radii such as non-Maxwellian distribution functions and pressure anisotropies. The aim of this research is to demonstrate the utility of the domain-decomposed hybrid method as described in Sec. 4 to capture the relevant physics by solving the kinetic model as described in Sec. 2.1 in the shear layer and the fluid model as described in Sec. 2.2 where the distribution functions are expected to remain close to Maxwellian. This allows for speedup in simulation times and reduction in computational costs by using the higher fidelity kinetic model only where it is needed.

This work is restricted to the study of the magnetized Kelvin-Helmholtz instability during linear growth. The low-beta property of the plasma studied means that the electrostatic assumption is valid and that results using the Vlasov-Maxwell and Vlasov-Poisson models should be indistinguishable [67]. The next sections describe the setup and results for simulations of the magnetized Kelvin-Helmholtz instability.

## 6.1. Vlasov-Maxwell equilibrium for the magnetized Kelvin-Helmholtz instability

The magnetized Kelvin-Helmholtz instability is simulated by initializing and perturbing an equilibrium that satisfies the Vlasov-Maxwell system as described in Sec. 2.1. The determination of the equilibrium for the Vlasov-Maxwell system closely follows the procedure outlined in Ref. [17], which determines an equilibrium for the Vlasov-Poisson system close to an equilibrium that satisfies the multi-fluid plasma model for electrons and ions for a specific density and electric field profile. The procedure outlined in Ref. [17] involves solving a nonlinear ordinary differential equation given by the Poisson equation that closely approximates the specified fluid density and electric field profiles, yielding solutions for the ion and electron distribution functions satisfying an equilibrium for the Vlasov-Poisson system. The determination of the kinetic equilibrium in this way is required for problems such as the magnetized Kelvin-Helmholtz instability, where Larmor radii and gradient scale lengths are comparable. In such cases, the fluid equilibrium becomes a poor approximation of the kinetic equilibrium, and thus initializing kinetic simulations using the fluid equilibrium can introduce spurious dynamics.

The following section summarizes the procedure to develop the kinetic equilibrium satisfying the Vlasov-Poisson system from the desired density and electric field profiles as described in Ref. [17], with a modification to satisfy the Vlasov-Maxwell system for low-beta plasmas.

## 6.1.1. Determining kinetic equilibria that satisfy the Vlasov-Maxwell system

The procedure for determining kinetic equilibria that satisfy the Vlasov-Poisson system begins by constructing auxiliary ion and electron distribution functions using constants of motion from specified ion density and electric field profiles from a two-fluid equilibrium. These auxiliary distribution functions are then used to solve a nonlinear Poisson equation to obtain exact equilibrium distribution functions, as described in detail in Refs. [17, 68].

The procedure can be understood through consideration of the Vlasov-Poisson system, consisting of Eq. (1) written for each species, and the Poisson equation, written in normalized form for electrostatic potential,  $\phi$ ,

$$-\frac{(\omega_c \tau)}{(\omega_p \tau)^2} \nabla^2 \phi = \sum_{\alpha} Z_{\alpha} n_{\alpha}, \tag{36}$$

where  $n_{\alpha}$  is the number density given by Eq. (6) for a species distribution function,  $f_{\alpha}$ . The problem of interest involves a two-species low-beta collisionless plasma with a one-dimensional equilibrium such that  $\phi = \phi(x)$  with a background magnetic field given by  $\mathbf{B} = B_z \hat{\mathbf{z}}$ . The Vlasov-Poisson equilibrium assumes that the background magnetic field is constant,  $B_z \equiv B_{z0} = 1$ . As described in Ref. [68], in such a plasma configuration, there exists two constants of motion, which are the energy and canonical momentum in the y-direction, written in normalized forms as

$$\mathcal{E}_{\alpha} = \frac{A_{\alpha} \left(v_x^2 + v_y^2\right)}{2T_{\alpha}} + \left(\omega_c \tau\right) \frac{Z_{\alpha} \phi(x)}{T_{\alpha}},\tag{37}$$

$$\mathcal{P}_{\alpha,y} = \frac{\mathcal{A}_y}{B_{z0}} + \frac{v_y}{\Omega_{c,\alpha}},\tag{38}$$

where

550

$$A_y = \int B_z dx \tag{39}$$

is the y-component of the magnetic vector potential, and  $\Omega_{c,\alpha}=(\omega_c\tau)\frac{Z_\alpha B_{z0}}{A_\alpha}$  is a normalized cyclotron frequency. The species distribution functions,  $f_\alpha$ , will satisfy Eq. (1) in equilibrium where  $\partial f_\alpha/\partial t=0$  if it can be expressed in terms of the constants of motion. Reference [68] assumes a form of  $f_\alpha$  where the canonical momentum and energy dependencies are multiplicatively separable, given by

$$f_{\alpha}(\mathcal{P}_{\alpha,y}, \mathcal{E}_{\alpha}) = N_{\alpha}(\mathcal{P}_{\alpha,y}) \frac{A_{\alpha}}{2\pi T_{\alpha}} \exp\left(-\mathcal{E}_{\alpha}\right)$$
(40)

for some function  $N(\mathcal{P}_{\alpha,y})$ . If the distribution functions for each species can be formulated in this way and their moments of Eq. (6) for  $n_{\alpha}$  additionally satisfy Eq. (36), a kinetic equilibrium for

the Vlasov-Poisson system can be found. Investigation of the relationship between  $n_{\alpha}$  and  $\mathcal{P}_{\alpha,y}$  in Ref. [68] shows that  $N(\mathcal{P}_{\alpha,y})$  can be expressed

$$N_{\alpha}(\mathcal{P}_{\alpha,y}) = \left[ g_{\alpha}(X) \exp\left( (\omega_c \tau) \frac{Z_{\alpha} \phi^*(X)}{T_{\alpha}} \right) \right]_{X = \mathcal{P}_{\alpha,y}}, \tag{41}$$

where  $g_{\alpha}(x)$  and  $\phi^*(x)$  are the desired density and electrostatic potential profiles that satisfy the specified fluid equilibrium. The Vlasov-Poisson equilibrium is then given by the solution for  $\phi(x)$  in Eq. (37) that upon substitution along with Eq. (41) into Eq. (40), yields plasma densities according to Eq. (6) that solve Eq. (36).

Defining auxiliary distribution functions facilitates determination of the solution to Eq. (36) by allowing an alternative form of Eq. (40) expressed as

$$f_{\alpha} = f_{\alpha}^{\text{aux}} \exp\left(\left(\omega_{c}\tau\right) \frac{Z_{\alpha} \left(\phi^{*} - \phi\right)}{T_{\alpha}}\right). \tag{42}$$

A similar relationship holds for the equilibrium number density, such that

$$n_{\alpha} = n_{\alpha}^{\text{aux}} \exp\left(\left(\omega_{c} \tau\right) \frac{Z_{\alpha} \left(\phi^{*} - \phi\right)}{T_{\alpha}}\right), \tag{43}$$

where  $n_{\alpha}^{\text{aux}}$  is calculated from  $f_{\alpha}^{\text{aux}}$  using Eq. (6). For a two-species ion-electron plasma with a specified equilibrium fluid ion density profile,  $g_{i}(x)$ , and electrostatic potential,  $\phi^{*}(x)$ , substitution of Eqs. (40) and (41) into Eq. (42) yields

$$f_{i}^{\text{aux}} = \left[ g_{i}(X) \exp\left( (\omega_{c} \tau) \frac{Z_{i} \phi^{*}(X)}{T_{i}} \right) \right]_{X = \mathcal{P}.} \frac{A_{i}}{2\pi T_{i}} \exp\left( -\frac{A_{i} \left( v_{x}^{2} + v_{y}^{2} \right)}{2T_{i}} - (\omega_{c} \tau) \frac{Z_{i} \phi^{*}(x)}{T_{i}} \right)$$
(44)

 $_{585}$  for ions, and

$$f_{\rm e}^{\rm aux} = \left[ -\frac{1}{Z_{\rm e}} \left( Z_{\rm i} n_{\rm i}^{\rm aux, fit}(X) + \frac{(\omega_c \tau)}{(\omega_p \tau)^2} \frac{\partial^2 \phi^*(X)}{\partial X^2} \right) \exp\left( (\omega_c \tau) \frac{Z_{\rm e} \phi^*(X)}{T_{\rm e}} \right) \right]_{X = \mathcal{P}_{\rm e, y}}$$

$$\times \frac{A_{\rm e}}{2\pi T_{\rm e}} \exp\left( -\frac{A_{\rm e} \left( v_x^2 + v_y^2 \right)}{2T_{\rm e}} - (\omega_c \tau) \frac{Z_{\rm e} \phi^*(x)}{T_{\rm e}} \right)$$

$$(45)$$

for electrons. In Eq. (45),  $g_e$  is written as the solution for  $n_e$  to Eq. (36) calculated from  $\phi^*(X)$  and  $n_i^{\text{aux}}(X)$ , where  $X = \mathcal{P}_{e,y}$ . A spline fit as described in Ref. [68] is constructed to evaluate  $n_i^{\text{aux}}(X)$ , which is evaluated numerically from  $f_i^{\text{aux}}$  using Eq. (6). After a similar evaluation of  $n_e^{\text{aux}}$ , Eq. (36) becomes

$$-\frac{(\omega_c \tau)}{(\omega_p \tau)^2} \frac{\partial^2 \phi}{\partial x^2} = Z_{\rm i} n_{\rm i}^{\rm aux} \exp\left((\omega_c \tau) \frac{Z_{\rm i} (\phi^* - \phi)}{T_{\rm i}}\right) + Z_{\rm e} n_{\rm e}^{\rm aux} \exp\left((\omega_c \tau) \frac{Z_{\rm e} (\phi^* - \phi)}{T_{\rm e}}\right). \tag{46}$$

Equation (46) can be solved numerically for  $\phi$  by discretizing the Laplacian operator and applying Newton's method. Details of entire procedure for finding the solution for  $\phi(x)$  are found in Ref. [68]. The computed distribution functions along with  $\phi(x)$  define the Vlasov-Poisson equilibrium using the fluid profiles  $g_i(x)$  and  $\phi^*(x)$  for a constant  $B_{z0}$ .

For the Vlasov-Maxwell system to satisfy equilibrium, the steady-state Ampere's Law, Eq. (2), should additionally be satisfied. Integration of the steady-state form of Eq. (2) yields the required magnetic field profile,

$$B_z(x) = B_z(x_0) - (\omega_c \tau) \int_{x_0}^x Z_i n_i(x) v_{iy}(x) + Z_e n_e(x) v_{ey}(x) dx, \tag{47}$$

where Eq. (7) is used and  $B_z(x_0) \equiv B_{z,x_0}$  is the magnetic field at a specified location. Evaluation of Eq. (47) yields a magnetic field consistent with the solution to  $\phi$  solved in Eq. (46), which, for electrostatic low-beta plasmas, should be close to the constant  $B_{z0}$ . However, the  $B_z(x)$  profile calculated in Eq. (47) can be integrated using Eq. (39) to calculate a corrected, self-consistent profile for  $A_y(x)$  in Eq. (38) and the process for finding the solution for  $\phi(x)$  can be repeated using the corrected  $A_y(x)$ . In this way, an equilibrium is found for the Vlasov-Maxwell system for a low-beta plasma for a self-consistent, nonuniform  $B_z(x)$  profile that approximates a uniform  $B_{z,x_0}$ . The next section applies this procedure for a specific initialization of the magnetized Kelvin-Helmholtz instability.

## 6.1.2. Vlasov-Maxwell equilibrium for the magnetized Kelvin-Helmholtz instability

The magnetized Kelvin-Helmholtz instability is initialized for the case of a two-species plasma with ions and electrons. The ion number density and electrostatic potential profiles that solve the fluid equilibrium as described in Ref. [17] are given by

$$g_{\mathbf{i}}(x) = \left[1 + \exp\left(\frac{2x}{d}\right)\right]^{\frac{bd}{2}} \tag{48}$$

610 and

$$\phi^*(x) = -\frac{E_{x,0}d}{2}\ln\left[1 + \exp\left(\frac{2x}{d}\right)\right],\tag{49}$$

where b, d and  $E_{x,0}$  are simulation parameters specifying an exponential growth factor, shear layer half-width, and electric field strength, respectively.

The procedure outlined in Sec. 6.1.1 to determine an equilibrium consistent with the Vlasov-Maxwell system is applied to case A1 as described in Ref. [17], where b = -10.0, d = 0.05 and  $E_{x,0} = 2.00 \times 10^{-2}$ . Additional parameters are  $\omega_p \tau = \omega_c \tau = 1$ , with  $m_0 = m_p$  and  $T_i = T_e = 6.25 \times 10^{-4}$ . The equilibrium is one-dimensional with  $x \in [-L_x/2, L_x/2]$  where  $L_x = 1.0$ . The magnetic field strength at  $x_0 = 0$  is  $B_{z,x_0} = 1.00$ , which is the starting point for the initial condition calculation in Sec. 6.1.1. The ion to electron mass ratio is set to  $A_i/A_e = 25$ . A comparison of  $\phi$  and  $A_y$  for the electrostatic case (calculating the equilibrium once based on  $B_z = B_{z,x_0}$ ) and the electromagnetic case (calculating the equilibrium using Eq. (47) as an input for a second iteration) is shown in Fig. 14. The equilibrium is solved using 512 grid points and second-order differencing. Since the equilibrium is for a low-beta plasma, the electrostatic and electromagnetic profiles are similar. Plots of n,  $v_y$ , T,  $E_x$ , and  $B_z$  in Fig. 15 demonstrate the similarities between these profiles.

# 6.2. Domain-decomposed hybrid simulations of the magnetized Kelvin-Helmholtz instability

The one-dimensional equilibrium calculated in Sec. 6.1.2 is used to initialize a simulation of the magnetized Kelvin-Helmholtz instability in two dimensions. The simulation parameters and discussion of results are described in the following subsections.

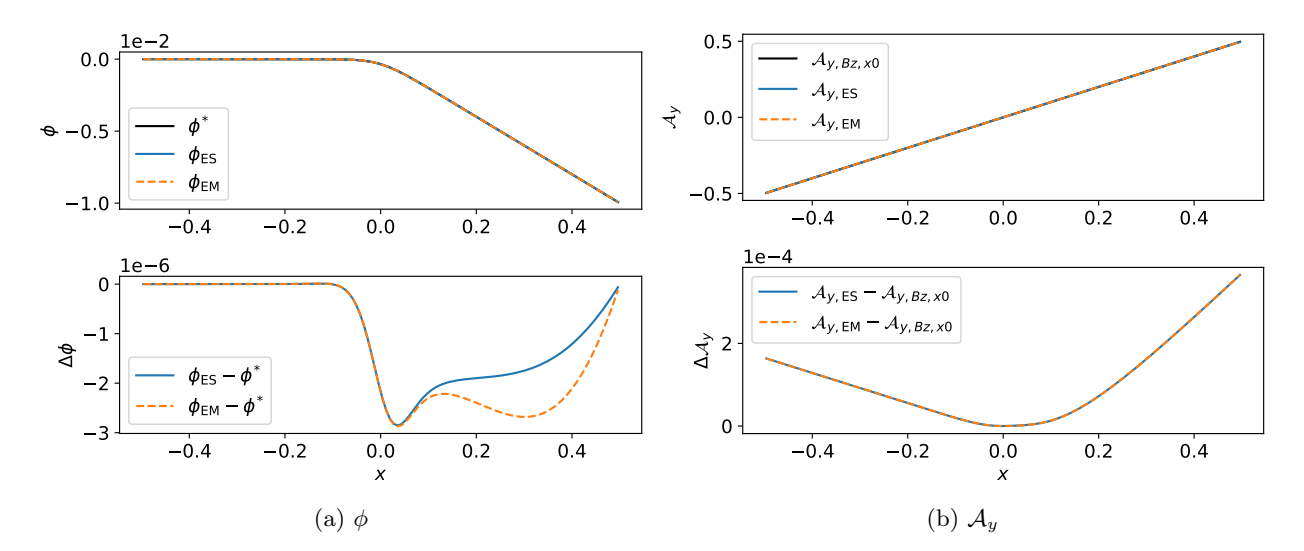


Figure 14: Profiles of the electrostatic scalar potential and the magnetic vector potential calculated for the initial condition for the magnetized Kelvin-Helmholtz instability. Potentials  $\phi^*$  and  $\mathcal{A}_{y,Bz,x0}$  satisfy the fluid equilibrium. Electrostatic quantities (ES) are calculated by deriving the initial condition for the Vlasov-Poisson system. Electromagnetic quantities (EM) are derived by additionally calculating a self-consistent, nonuniform  $B_z$  profile according to Eq. (47), calculating the corresponding magnetic vector potential using Eq. (39), and recalculating the equilibrium. Since the equilibrium system is for a low-beta plasma, the electrostatic and electromagnetic profiles are similar.

#### 6.2.1. Initial conditions for the magnetized Kelvin-Helmholtz instability

Simulations of the magnetized Kelvin-Helmholtz instability evolved from the perturbed equilibrium derived in Sec. 6.1.2 are performed on a two-dimensional physical-space domain of  $x \in$  $[-L_x/2, L_x/2]$  and  $y \in [-L_y/2, L_y/2]$  where  $L_y = 2\pi/k_y$  with  $k_y = 8$ . The domain is subdivided into a middle subdomain with  $x \in [-L_x/4, L_x/4]$ , an outside subdomain to the left with  $x \in [-L_x/2, -L_x/4]$ , and an outside subdomain to the right with  $x \in [L_x/4, L_x/2]$ . The physicalspace grid for the entire domain is composed of  $32 \times 16$  second-order polynomial basis function triangular elements, which are created from a subdivision of each element in a  $32 \times 8$  rectangular grid. Dirichlet boundary conditions on the left and right walls are used, setting all variables to the initial condition, and periodic boundary conditions are used at the top and bottom of the domain. A simulation is performed using the Vlasov-Maxwell kinetic model described in Sec. 2.1 over the entire domain for both ions and electrons, which in the remainder of this section is referred to as the kinetic simulation. A simulation is also performed in which the ions are solved using the Vlasov-Maxwell kinetic model in the middle subdomain and the fluid model described in Sec. 2.2 in the left and right subdomains while the electrons are solved using the Vlasov-Maxwell kinetic model in all subdomains. This is referred to as the hybrid simulation in the remainder of this section. In the subdomains in which the kinetic model is used, the velocity space is comprised of two velocity dimensions, such that  $v_x, v_y \in [-v_{\max,\alpha}, v_{\max,\alpha}]$  where  $v_{\max,e} = 1.0$  and  $v_{\max,i} = 0.2$ . The velocity space is discretized using  $32 \times 32$  second-order polynomial basis function rectangular elements. The phase-space elements are constructed from tensor products of the underlying triangular elements in physical space and rectangular elements in velocity space, yielding 3-4 duoprism elements [69]. In the left and right subdomains where the fluid model is solved for the ions, initial values for fluid variables are calculated from velocity moments in Eqs. (6), (7), and (8) of the initialized equilibrium distribution functions. Values of  $\chi_i$  in the left and right subdomains at the

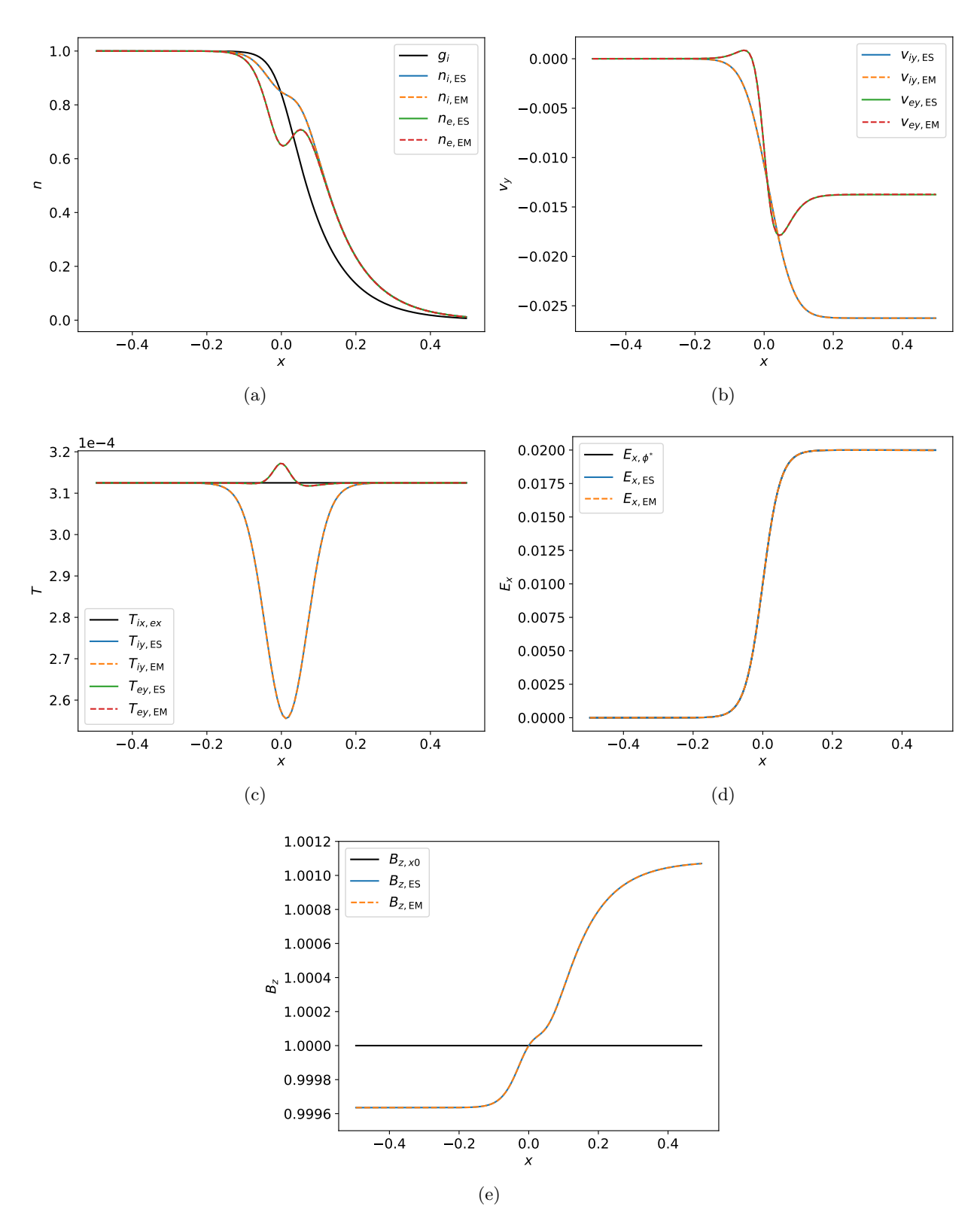


Figure 15: Profiles of n,  $v_y$ , T,  $E_x$ , and  $B_z$  for the initial condition for the magnetized Kelvin-Helmholtz instability, calculated under electrostatic and electromagnetic assumptions. Figure 15e shows the correction to the constant  $B_z$  that satisfies Eq. (47). The electrostatic and electromagnetic profiles are similar, which is expected for the low-beta plasma equilibrium.

initial condition are found to be below  $10^{-4}$ , validating the fluid model. Rusanov fluxes are used in the fluid subdomains and for consistency with 2 degrees of freedom in a 2D2V simulation, the adiabatic index is set to  $\gamma = 2$ . To seed the instability, a perturbation is applied to the electron distribution function as described in Ref. [17], which multiplies  $f_e$  by a factor  $(1 + \epsilon)$ , where

$$\epsilon = 2.0 \times 10^{-4} \sin\left(k_y y\right) \exp\left(-\frac{x^6}{d^6}\right). \tag{50}$$

Third-order ERK timestepping is used to advance solutions until a time of  $t\omega_s = 60$ , for which linear behavior is expected. The shearing rate,  $\omega_s$ , is related to the ion velocity jump in the shear layer,  $\Delta v_{iy}(t=0)$  in Fig. 15b, through the relationship  $\omega_s = |\Delta v_{iy}(t=0)|/(2d)$ . Reference [17] approximates  $\Delta v_{iy}(t=0) = -0.02625$  for case A1, leading to  $\omega_s = 0.2625$ .

A hybrid simulation using the fluid model for both the electrons and ions in the left and right subdomains coupled to the kinetic model in the middle subdomain is also performed. However, this simulation loses accuracy due to the electron distribution function developing large deviations from a Maxwellian over the entire domain as evidenced by large values of  $\chi_e$ . Therefore, results from this simulation are not included in the investigation.

## 6.2.2. Simulation results of the magnetized Kelvin-Helmholtz instability

685

A plot of the evolution of the ion transverse velocity in the x-direction at (x,y)=(0,0) is shown in Fig. 16 for the kinetic and hybrid simulations. The linear growth rate from the hybrid simulation is calculated to be  $\omega_i/\omega_s=0.1485$ , compared to  $\omega_i/\omega_s=0.1527$  for the kinetic simulation, based on line fits of the peaks between  $t\omega_s=20$  and  $t\omega_s=50$  before effects of nonlinear saturation are observed. These growth rates are within 5.3% of the growth rate of  $\omega_i/\omega_s=0.145$  found for the Vlasov-Poisson simulation in Ref. [17]. The growth rates shown in Fig. 16 approximate the kinetic simulation results markedly better than two-fluid simulation results, which has  $\omega_i/\omega_s=0.174$  [17].

Figure 17 shows the ion number density for each simulation measured at  $t\omega_s=60$ . There are some discontinuities at the model interfaces at  $x/d=\pm 5$  in the hybrid simulation. Figure 18 shows  $\chi_i$  for the kinetic and hybrid simulations at  $t\omega_s=60$ . The kinetic simulation shows  $\chi_i$  to be approximately between 0.01-0.02 at the x/d=-5 interface and approximately between 0.02-0.03 at the x/d=5 interface, indicating deviation from Maxwellian at these levels are sufficient to cause the ion number density discontinuities. Values of  $\chi_i$  in the hybrid simulation show that the differences in the kinetic and Maxwellian distribution functions on the x/d=5 interface where density is low further increases the Maxwellian deviation. Thus, it may be advantageous to extend the kinetic subdomain beyond x/d=5 where  $\chi_i$  is lower to reduce the discontinuities, as is performed for the plasma sheath in Sec. 5.2. An investigation of the effect of this extension of the kinetic subdomain is a topic of future research.

Figure 19 measures mass, y-momentum, and energy for ions integrated over the physical domain for the hybrid simulation relative to the kinetic simulation. Similar to Eqs. (33) and (34) in Sec. 5.2, these integrations in two dimensions are

$$\frac{\Delta M}{M_K} = \left| \frac{\int \rho(t)dA - \int \rho_K(t)dA}{\int \rho_K(t)dA} \right|,\tag{51}$$

$$\frac{\Delta P_y}{P_{y,K}} = \left| \frac{\int p_y(t)dA - \int p_{y,K}(t)dA}{\int p_{y,K}(t)dA} \right|,\tag{52}$$

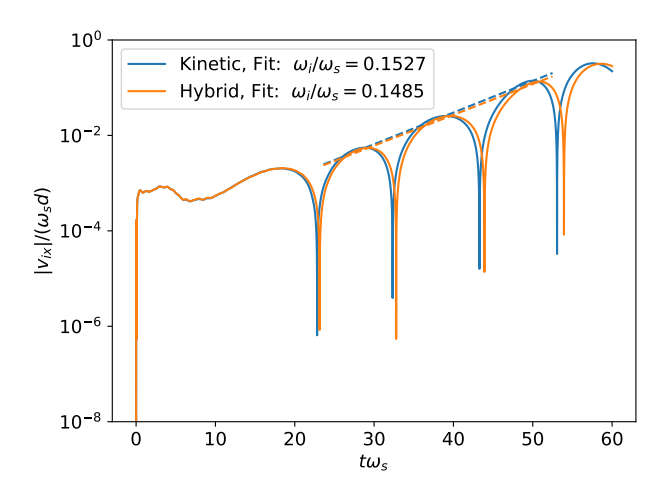


Figure 16: Evolution of the ion transverse velocity in the x-direction,  $v_{ix}$ , at (x,y)=(0,0), plotted as  $\frac{|v_{ix}|}{\omega_s d}$  versus  $t\omega_s$  for the kinetic and hybrid simulations using  $32\times16\times32\times32$  second-order polynomial phase-space elements and third-order explicit Runge-Kutta timestepping. Growth rates of the instability are calculated by fitting a line through the peaks between  $t\omega_s=20$  and  $t\omega_s=50$  before nonlinear saturation occurs. The initial conditions for both simulations are calculated from a kinetic equilibrium consistent with the Vlasov-Maxwell system. In subdomains where the fluid equations are solved, the equilibrium distribution functions are transformed to Maxwellians to initialize the fluid moment variables. The evolution of  $v_{ix}$  in both simulations is similar, indicating the ability of the hybrid method to accurately capture the relevant physical phenomena.

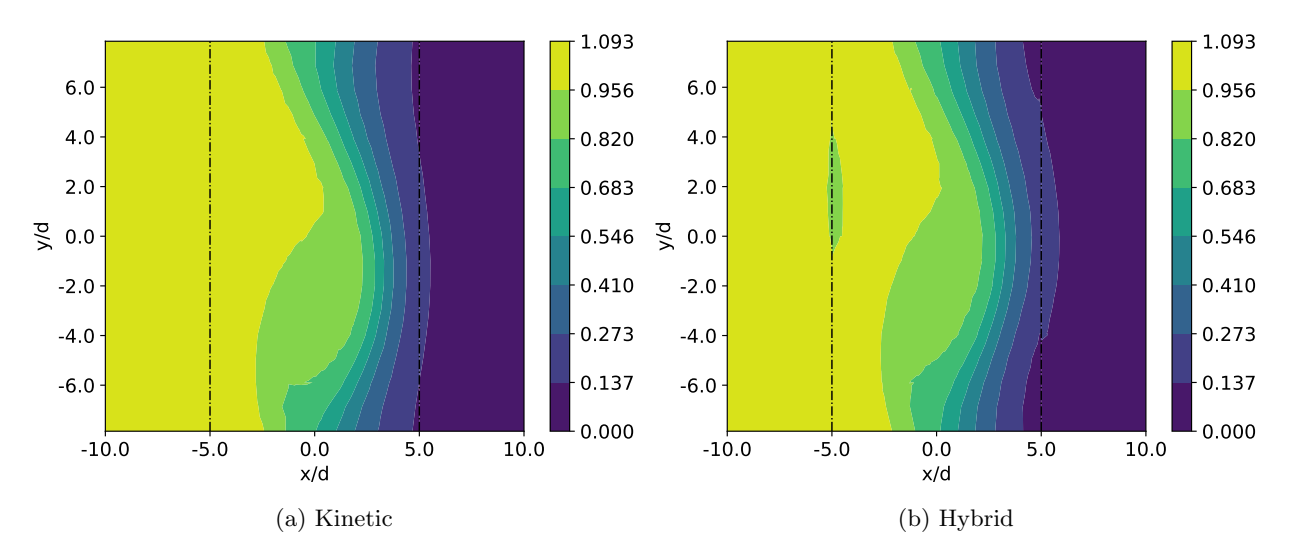


Figure 17: Contours of the ion number density,  $n_i(x, y)$ , for the magnetized Kelvin-Helmholtz instability at  $t\omega_s = 60$  compared for the kinetic and hybrid simulations. Some discontinuities do appear at the subdomain interfaces at  $x/d = \pm 5$ .

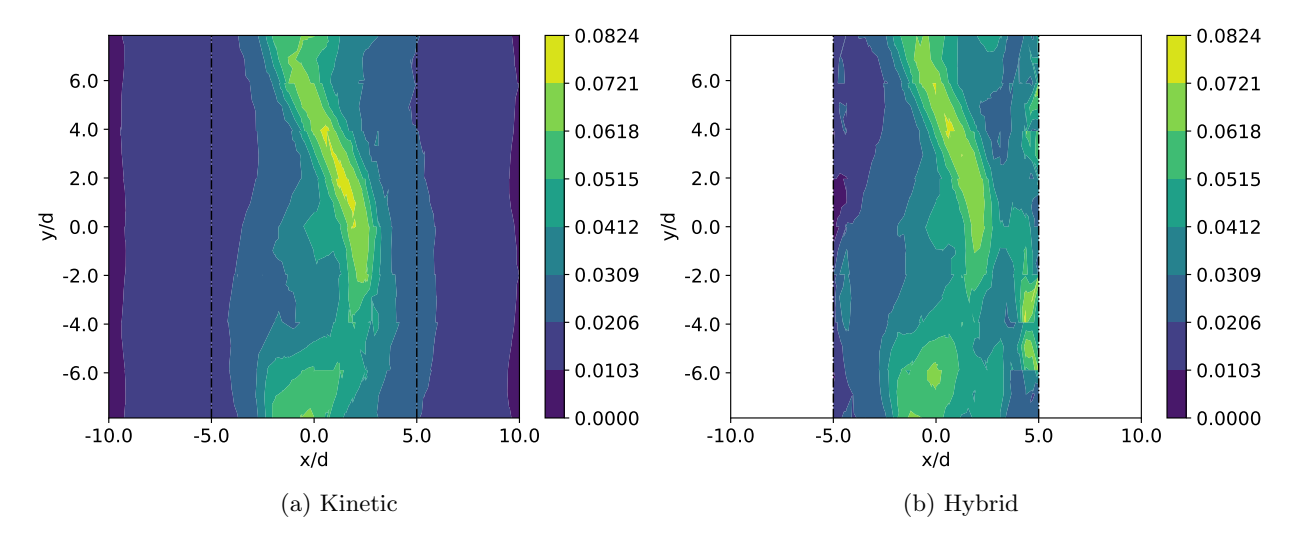


Figure 18: Contours of  $\chi_i(x,y)$  for the magnetized Kelvin-Helmholtz instability at  $t\omega_s=60$  compared for the kinetic and hybrid simulations. The  $\chi_i$  measurement is performed for  $x/d \in [-10,10]$  in the kinetic simulation and for  $x/d \in [-5,5]$  in the hybrid simulation where the Vlasov-Maxwell equations are solved. The discontinuities in  $n_i(x,y)$  in Fig. 18b at the subdomain interfaces can be explained by the  $\chi_i$  values at those locations. The Maxwellian deviation is also exacerbated in the hybrid simulation especially at the x/d=5 subdomain interface.

$$\frac{\Delta E}{E_K} = \left| \frac{\int e(t)dA - \int e_K(t)dA}{\int e_K(t)dA} \right|. \tag{53}$$

As with the 1D1V conservation calculations in Sec. 5.2, Eqs. (51), (52), and (53) help to assess the performance of the hybrid simulation using the domain-decomposed hybrid method. Integrated x-momentum is maintained at zero for both the kinetic and hybrid simulations. Figure 19 shows that conservation in the hybrid simulation reduces as the simulation progresses and the instability grows. This is due to increasing deviations from Maxwellian in the subdomain interface distribution functions, observed through increasing values of  $\chi_i$  over time. This behavior suggests the need for extending the kinetic subdomain if simulations are run to a longer time. The subdomains could also be changed dynamically during the simulation, where the kinetic subdomain is expanded or contracted based on measured values of  $\chi_i$ , or on locally evaluated collisionality, magnetization, charge separation, or pressure anisotropy.

Further simulations using higher order elements and higher resolution may be desirable to further resolve the instability and calculate convergence of the growth rate. However, the simulations presented in this section show the viability of the domain-decomposed hybrid method, particularly using direct variable translation, as a means to reduce the computational cost by using the fluid model in regions where the distribution function remains close to a Maxwellian.

700

705

The hybrid simulation, which applies the fluid model for ions on half of the domain, reduces the simulation time by 28% with a memory saving of 25%. In both simulations, the domain is divided into approximately equal areas in physical space on which different compute nodes communicating using MPI advance the solution in parallel. Additional speedup can thus be realized for the hybrid simulation with the use of load balancing measures, such as by applying more compute nodes to the kinetic subdomain, where the more computationally expensive kinetic model is used to advance

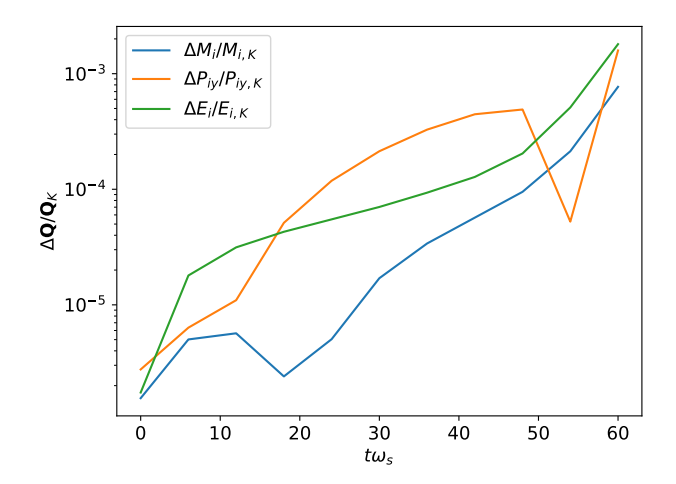


Figure 19: Mass, y-momentum, and energy integrated over the physical domain for the hybrid simulation relative to the kinetic simulation,  $\Delta \mathbf{Q}/\mathbf{Q}_K = [\Delta M/M_K, \Delta P_y/P_{y,K}, \Delta E/E_K]$  as described in Eqs. (51), (52), and 53, calculated for ions for the magnetized Kelvin-Helmholtz instability. Calculations are performed at intervals of  $t\omega_s = 6$ . As the instability develops, the values of  $\chi_i$  at the subdomain interfaces increase and larger differences between the hybrid and kinetic simulation results are observed, such as the integrated mass, y-momentum, and energy.

the solution for ions.

The approach of coupling two plasma models with different physical fidelity to improve computational efficiency without sacrificing physical accuracy can be extended by including plasma models of intermediate fidelity to smooth the transitions between the multi-species kinetic and multi-fluid models. For example, a 13N-moment model which accounts for anisotropies in the distribution function in a weakly collisional regime [15] could be applied where direct variable translation or a form of the composite distribution function method could be used to couple the kinetic model to the higher moment model at one interface of the intermediate subdomain and a similar formulation could be used to couple the higher moment model to the 5N-moment model at the other interface. Such an approach may help to reduce the discrepancies seen at the subdomain interfaces in the sheath simulations as well as those of the Kelvin-Helmholtz instability and would make the transition from the continuum kinetic model to the 5N-moment model gradual through fluid models of higher validity for non-Maxwellian distribution functions. Extending the domain-decomposed hybrid method to include plasma models of intermediate fidelity is a topic of future research.

## 7. Conclusions

This research presents the domain-decomposed hybrid method for simulations coupling the multi-fluid plasma model and the multi-species kinetic model governing plasma dynamics in the presence electromagnetic fields, enabling faster simulations with reduced computational resources while maintaining high physical fidelity. The method subdivides a simulation domain into separate subdomains in which the different models are solved. The solution for each model is calculated using the same continuum method, the discontinuous Galerkin finite element method, which facilitates the specification of the interface conditions between the different models on adjacent subdomains. The specification of these interface conditions is defined through surface numerical fluxes, which are a component of the discontinuous Galerkin method. The domain-decomposed hybrid method

can be applied separately for different species such as ions and electrons, which is advantageous for many applications where the fluid approximation may be sufficient to govern the dynamics of one species but not another.

Two particular methods are studied for specification of the numerical flux at subdomain interfaces. The first method, called the direct variable translation method, constructs fluid variables from the kinetic distribution function at a subdomain interface. The construction of the fluid variables from the kinetic distribution function allows for determination of the numerical flux for the multi-fluid plasma model in a manner that is consistent with the fluid approximation of Maxwellian distribution functions. The second method, called the composite distribution function method, calculates numerical fluxes based on the construction of a composite distribution function at the subdomain interface, ensuring conservation of the distribution function as well as mass, momentum, and energy.

The direct variable translation and composite distribution function methods are tested using simulations of a double rarefaction wave and a plasma sheath using the multi-fluid plasma model in 1D and the multi-species kinetic model in 1D1V. Results demonstrate the conservation properties of each method and show good coupling results for distribution functions on either side of a subdomain interface approaching a common Maxwellian. The effectiveness of the coupling reduces when the distribution function at the subdomain interface deviates from a Maxwellian, which can be measured using the metric,  $\chi$ . In such cases, accumulation along with increased oscillatory behavior of the distribution function emanating from the subdomain interfaces can occur. Placing the subdomain interfaces at locations of lower  $\chi$  improves the solution accuracy and resolves the numerical artifacts. The direct variable translation method, despite having weaker conservation properties, is found to be more robust than the composite distribution function method due to reduced numerical artifacts at subdomain interfaces for a given value of  $\chi$ .

The direct variable translation method is then used to couple ions simulated using the multi-fluid plasma model in 2D and the multi-species kinetic model in 2D2V for the magnetized Kelvin-Helmholtz instability. An equilibrium is initialized that satisfies the steady-state electromagnetic Vlasov-Maxwell system, modified from a method deriving the Vlasov-Poisson equilibrium for electrostatics. The hybrid simulation yields a linear growth rate of the instability that agrees well with a simulation using the kinetic model with no hybridization, but does so in less time and with memory savings, consistent with the reduced computational complexity of the multi-fluid plasma model compared with the multi-species kinetic model. The ability to capture the relevant physical phenomena with reduced computational resources demonstrates the viability of the domain-decomposed hybrid method for the simulation of plasma dynamics to high physical fidelity.

Further advancement in the method presented in this work for hybridization of the fluid and kinetic models are suggested. The domain decomposition can be made dynamic, such that subdomain interface locations evolve throughout a simulation based on local plasma parameters. The  $\chi$  metric could be used to determine dynamic decomposition, so that the subdomain interfaces move to where  $\chi$  is below a specified level, applying the fluid model only in regions where it is valid. Furthermore, the interface locations can be replaced with transition regions where the solutions to the fluid and kinetic models transition into each other over some finite distance, as described in Refs. [27, 28]. This could potentially reduce the numerical artifacts that occur at some subdomain interfaces. Additional load balancing measures such as dedication of more computational resources to subdomains where the more computationally intensive kinetic model is solved can increase computational efficiency and further reduce simulation time. Coupling the kinetic model to a higher

moment model in an intermediate subdomain between the kinetic and 5N-moment formulations may also help to maintain numerical stability and capture realistic physics where the distribution function is non-Maxwellian. This could be combined with dynamic domain decomposition, with parameters such as local mean free path, Larmor radius, Debye length, and pressure anisotropy serving as metrics for collisionality, magnetization, charge separation, and thermal equilibrium, respectively, which can be used to specify which plasma models to use in various regions of the domain. These improvements will help reduce the computational cost of simulating plasma dynamics to high fidelity, allowing for numerical simulation of phenomena beyond the current capabilities.

# Acknowledgements

The authors would like to thank D. W. Crews, A. Ho, E. T. Meier, and G. V. Vogman for stimulating discussions. The information, data, or work presented herein was funded in part by the Air Force Office of Scientific Research under award numbers FA9550-15-1-0271. This material is also based upon work supported by the National Science Foundation under Grant No. PHY-2108419.

#### 795 References

800

810

- U. Shumlak, Z-pinch fusion, Journal of Applied Physics 127 (20) (2020) 200901.
   URL https://doi.org/10.1063/5.0004228
- [2] C. K. Lau, D. P. Fulton, J. Bao, Z. Lin, S. Dettrick, M. Binderbauer, T. Tajima, L. Schmitz, Electrostatic quasi-neutral formulation of global cross-separatrix particle simulation in field-reversed configuration geometry, Physics of Plasmas 27 (2020) 082504. URL https://doi.org/10.1063/5.0012439
- [3] S. A. Slutz, R. A. Vesey, High-Gain Magnetized Inertial Fusion, Physical Review Letters 108 (2) (2012) 025003. URL https://doi.org/10.1103/PhysRevLett.108.025003
- [4] P. Rodriguez-Fernandez, N. T. Howard, M. J. Greenwald, A. J. Creely, J. W. Hughes, J. C. Wright, C. Holland, Y. Lin, F. Sciortino, the SPARC Team, Predictions of core plasma performance for the SPARC tokamak, Journal of Plasma Physics 86 (5) (2020) 865860503. URL https://doi.org/10.1017/S0022377820001075
  - [5] I. D. Boyd, Simulation of Electric Propulsion Thrusters, Tech. Rep. EN-AVT-194-17, University of Michigan, Ann Arbor, MI, USA (2011).
    - URL https://apps.dtic.mil/sti/pdfs/ADA587239.pdf
  - [6] J.-P. Boeuf, Tutorial: Physics and modeling of Hall thrusters, Journal of Applied Physics 121 (2017) 011101.URL https://doi.org/10.1063/1.4972269
  - [7] J. Leenaarts, Radiation hydrodynamics in simulations of the solar atmosphere, Living Reviews in Solar Physics 17 (3) (2020) 1–46.
    - ${\rm URL\ https://doi.org/10.1007/s41116-020-0024-x}$
  - [8] G. Tóth, Y. Chen, Z. Huang, B. van der Holst, Challenges in Modeling the Outer Magnetosphere, in: R. Maggiolo, N. André, H. Hasegawa, D. T. Welling, Y. Zhang, L. J. Paxton (Eds.), Magnetospheres in the Solar System, Geophysical Monograph Series, American Geophysical Union (AGU), 2021, Ch. 44, pp. 715–728. URL https://doi.org/10.1002/9781119815624.ch44
- [9] T. I. Gombosi, Y. Chen, A. Glocer, Z. Huang, X. Jia, M. W. Liemohn, W. B. Manchester, T. Pulkkinen, N. Sachdeva, Q. A. Shidi, I. V. Sokolov, J. Szente, V. Tenishev, G. Toth, B. van der Holst, D. T. Welling, L. Zhao, S. Zou, What sustained multi-disciplinary research can achieve: The space weather modeling framework, Journal of Space Weather and Space Climate 11 (42) (2021) 1–55.
  URL https://doi.org/10.1051/swsc/2021020
- 825 [10] M. W. Kunz, J. M. Stone, X.-N. Bai, Pegasus: A new hybrid-kinetic particle-in-cell code for astrophysical plasma dynamics, Journal of Computational Physics 259 (2014) 154–174. URL https://doi.org/10.1016/j.jcp.2013.11.035

- [11] J. E. Borovsky, G. L. Delzanno, Active Experiments in Space: The Future, Frontiers in Astronomy and Space Sciences 6 (2019) 31.
  - URL https://doi.org/10.3389/fspas.2019.00031

830

845

855

865

875

- [12] U. Shumlak, J. Loverich, Approximate Riemann solver for the two-fluid plasma model, Journal of Computational Physics 187 (2) (2003) 620–638.
  - URL https://doi.org/10.1016/S0021-9991(03)00151-7
- [13] U. Shumlak, R. Lilly, N. Reddell, E. Sousa, B. Srinivasan, Advanced physics calculations using a multi-fluid plasma model, Computer Physics Communications 182 (9) (2011) 1767–1770.

  URL https://doi.org/10.1016/j.cpc.2010.12.048
  - [14] A. H. Hakim, Extended MHD Modelling with the Ten-Moment Equations, Journal of Fusion Energy 27 (1-2) (2007) 36–43.
    - URL https://doi.org/10.1007/s10894-007-9116-z
- 840 [15] S. T. Miller, U. Shumlak, A multi-species 13-moment model for moderately collisional plasmas, Physics of Plasmas 23 (8) (2016) 082303. URL https://doi.org/10.1063/1.4960041
  - [16] F. Filbet, E. Sonnendrücker, Comparison of Eulerian Vlasov solvers, Computer Physics Communications 150 (3) (2003) 247–266.
    - URL https://doi.org/10.1016/S0010-4655(02)00694-X
  - [17] G. V. Vogman, J. H. Hammer, U. Shumlak, W. A. Farmer, Two-fluid and kinetic transport physics of Kelvin-Helmholtz instabilities in nonuniform low-beta plasmas, Physics of Plasmas 27 (2020) 102109. URL https://doi.org/10.1063/5.0014489
- [18] G. Vogman, U. Shumlak, P. Colella, Conservative fourth-order finite-volume Vlasov-Poisson solver for axisymmetric plasmas in cylindrical (r, v, v) phase space coordinates, Journal of Computational Physics 373 (2018) 877–899.
  - URL https://doi.org/10.1016/j.jcp.2018.07.029
  - [19] N. Reddell, A Kinetic Vlasov Model for Plasma Simulation Using Discontinuous Galerkin Method on Many-Core Architectures, Ph.D. thesis, University of Washington, Seattle, WA (2016).
  - URL https://www.aa.washington.edu/sites/aa/files/faculty/shumlak/research/cpdlab/docs/reddell\_noah\_dissertation.pdf
  - [20] J. Juno, A. Hakim, J. TenBarge, E. Shi, W. Dorland, Discontinuous Galerkin algorithms for fully kinetic plasmas, Journal of Computational Physics 353 (2018) 110-147. URL https://doi.org/10.1016/j.jcp.2017.10.009
- [21] J. W. Banks, J. A. F. Hittinger, A New Class of Nonlinear Finite-Volume Methods for Vlasov Simulation, IEEE Transactions on Plasma Science 38 (9) (2010) 2198 – 2207. URL https://doi.org/10.1109/TPS.2010.2056937
  - [22] J. Hittinger, J. Banks, Block-structured adaptive mesh refinement algorithms for Vlasov simulation, Journal of Computational Physics 241 (2013) 118–140.
  - URL https://doi.org/10.1016/j.jcp.2013.01.030
  - [23] G. L. Delzanno, Multi-dimensional, fully-implicit, spectral method for the Vlasov-Maxwell equations with exact conservation laws in discrete form, Journal of Computational Physics 301 (2015) 338-356. URL https://doi.org/10.1016/j.jcp.2015.07.028
- [24] S. Mijin, F. Militello, S. Newton, J. Omotani, R. J. Kingham, Kinetic and fluid simulations of parallel electron transport during equilibria and transients in the scrape-off layer, Plasma Physics and Controlled Fusion 62 (9) (2020) 095004.
  - URL https://doi.org/10.1088/1361-6587/ab9b39
  - [25] L. Carbajal, R. O. Dendy, S. C. Chapman, J. W. S. Cook, Linear and nonlinear physics of the magnetoacoustic cyclotron instability of fusion-born ions in relation to ion cyclotron emission, Physics of Plasmas 21 (2014) 012106.
    - URL https://doi.org/10.1063/1.4861866
  - [26] M. Palmroth, U. Ganse, Y. Pfau-Kempf, M. Battarbee, L. Turc, T. Brito, M. Grandin, S. Hoilijoki, A. Sandroos, S. von Alfthan, Vlasov methods in space physics and astrophysics, Living Reviews in Computational Astrophysics 4 (1) (2018).
    - URL https://doi.org/10.1007/s41115-018-0003-2
  - [27] P. Degond, S. Jin, A Smooth Transition Model between Kinetic and Diffusion Equations, SIAM Journal on Numerical Analysis 42 (6) (2005) 2671–2687.
    - URL https://doi.org/10.1137/S0036142903430414

- [28] P. Degond, S. Jin, L. Mieussens, A smooth transition model between kinetic and hydrodynamic equations,
   Journal of Computational Physics 209 (2) (2005) 665-694.
   URL https://doi.org/10.1016/j.jcp.2005.03.025
  - [29] J. M. Burt, I. D. Boyd, A hybrid particle approach for continuum and rarefied flow simulation, Journal of Computational Physics 228 (2009) 460-475. URL https://doi.org/10.1016/j.jcp.2008.09.022
- [30] J. W. Schumer, S. B. Swanekamp, P. F. Ottinger, R. J. Commisso, B. V. Weber, D. N. Smithe, L. D. Ludeking, MHD-to-PIC Transition for Modeling of Conduction and Opening in a Plasma Opening Switch, IEEE Transactions on Plasma Science 29 (3) (2001) 479–493. URL https://doi.org/10.1109/27.928946
  - [31] T. Sugiyama, K. Kusano, Multi-scale plasma simulation by the interlocking of magnetohydrodynamic model and particle-in-cell kinetic model, Journal of Computational Physics 227 (2) (2007) 1340–1352. URL https://doi.org/10.1016/j.jcp.2007.09.011

895

900

- [32] L. K. Daldorff, G. Tóth, T. I. Gombosi, G. Lapenta, J. Amaya, S. Markidis, J. U. Brackbill, Two-way coupling of a global Hall magnetohydrodynamics model with a local implicit particle-in-cell model, Journal of Computational Physics 268 (2014) 236–254.
- URL https://doi.org/10.1016/j.jcp.2014.03.009
  [33] G. Tóth, X. Jia, S. Markidis, I. B. Peng, Y. Chen, L. K. S. Daldorff, V. M. Tenishev, D. Borovikov, J. D. Haiducek, T. I. Gombosi, A. Glocer, J. C. Dorelli, Extended magnetohydrodynamics with embedded particle-in-cell simulation of Ganymede's magnetosphere, Journal of Geophysical Research: Space Physics 121 (2) (2016) 1273–1293.
- URL https://doi.org/10.1002/2015ja021997
  [34] G. Tóth, Y. Chen, T. I. Gombosi, P. Cassak, S. Markidis, I. B. Peng, Scaling the Ion Inertial Length and Its Implications for Modeling Reconnection in Global Simulations, Journal of Geophysical Research: Space Physics 122 (10) (2017) 10,336-10,355.
  URL https://doi.org/10.1002/2017JA024189
- 910 [35] Y. Chen, G. Tóth, P. Cassak, X. Jia, T. I. Gombosi, J. A. Slavin, S. Markidis, I. B. Peng, V. K. Jordanova, M. G. Henderson, Global Three-Dimensional Simulation of Earth's Dayside Reconnection Using a Two-Way Coupled Magnetohydrodynamics With Embedded Particle-in-Cell Model: Initial Results, Journal of Geophysical Research: Space Physics 122 (10) (2017) 10,318–10,335.
  URL https://doi.org/10.1002/2017JA024186
- 915 [36] V. I. Kolobov, R. R. Arslanbekov, V. V. Aristov, A. A. Frolova, S. A. Zabelok, Unified solver for rarefied and continuum flows with adaptive mesh and algorithm refinement, Journal of Computational Physics 223 (2007) 589–608.
- URL https://doi.org/10.1016/j.jcp.2006.09.021
  [37] V. Kolobov, R. Arslanbekov, Towards adaptive kinetic-fluid simulations of weakly ionized plasmas, Journal of
  Computational Physics 231 (3) (2012) 839-869.
  URL https://doi.org/10.1016/j.jcp.2011.05.036
  - [38] S. Zabelok, R. Arslanbekov, V. Kolobov, Adaptive kinetic-fluid solvers for heterogeneous computing architectures, Journal of Computational Physics 303 (2015) 455-469.
    URL https://doi.org/10.1016/j.jcp.2015.10.003
- [39] R. Arslanbekov, V. Kolobov, Adaptive Kinetic-Fluid Models for Expanding Plasmas, Journal of Physics: Conference Series 1031 (012018) (2018) 1–13. URL https://doi.org/10.1088/1742-6596/1031/1/012018
  - [40] S. Lautenbach, R. Grauer, Multiphysics Simulations of Collisionless Plasmas, Frontiers in Physics 6 (2018) 113. URL https://doi.org/10.3389/fphy.2018.00113
- [41] Q. Sun, I. D. Boyd, G. V. Candler, A hybrid continuum/particle approach for modeling subsonic, rarefied gas flows, Journal of Computational Physics 194 (1) (2004) 256-277. URL https://doi.org/10.1016/j.jcp.2003.09.005
  - [42] A. Ho, I. A. M. Datta, U. Shumlak, Physics-Based-Adaptive Plasma Model for High-Fidelity Numerical Simulations, Frontiers in Physics 6 (2018) 105. URL https://doi.org/10.3389/fphy.2018.00105
  - [43] L. D. Landau, E. M. Lifshitz, Physical Kinetics, 1st Edition, Vol. 10 of Landau and Lifshitz: Course of Theoretical Physics, Pergamon Press Ltd., Oxford, UK, 1981.
  - [44] P. L. Bhatnagar, E. P. Gross, M. Krook, A Model for Collision Processes in Gases. I. Small Amplitude Processes in Charged and Neutral One-Component Systems, Physical Review 94 (3) (1954) 511–525.

URL https://doi.org/10.1103/PhysRev.94.511

940

- [45] E. T. Meier, U. Shumlak, A general nonlinear fluid model for reacting plasma-neutral mixtures, Physics of Plasmas 19 (072508) (2012) 1–11. URL https://doi.org/10.1063/1.4736975
- [46] J. Cheng, J. Dominski, H. C. Yang Chen, G. Merlo, S.-H. Ku, R. Hager, C.-S. Chang, E. Suchyta, E. D'Azevedo, S. Ethier, S. Sreepathi, S. Klasky, F. Jenko, A. Bhattacharjee, S. Parker, Spatial core-edge coupling of the particle-in- cell gyrokinetic codes GEM and XGC, Physics of Plasmas 27 (2020) 122510. URL https://doi.org/10.1063/5.0026043
  - [47] J. S. Hesthaven, T. Warburton, Nodal Discontinuous Galerkin Methods: Algorithms, Analysis, and Applications, Springer Science+Business Media, LLC, New York, USA, 2008.
- 950 [48] M. Brio, C. C. Wu, An Upwind Differencing Scheme for the Equations of Ideal Magnetohydrodynamics, Journal of Computational Physics 75 (2) (1988) 400–422.
  URL https://doi.org/10.1016/0021-9991(88)90120-9
  - [49] A. L. Zachary, P. Colella, A Higher-Order Godunov Method for the Equations of Ideal Magnetohydrodynamics, Journal of Computational Physics 99 (2) (1992) 341–347. URL https://doi.org/10.1016/0021-9991(92)90213-I
  - [50] O. S. Jones, U. Shumlak, D. S. Eberhardt, An Implicit Scheme for Nonideal Magnetohydrodynamics, Journal of Computational Physics 130 (2) (1997) 231–242. URL https://doi.org/10.1006/jcph.1996.5580
- [51] J. Loverich, U. Shumlak, A discontinuous Galerkin method for the full two-fluid plasma model, Computer
   Physics Communications 169 (1-3) (2005) 251-255.
   URL https://doi.org/10.1016/j.cpc.2005.03.058
  - [52] J. Loverich, A. Hakim, U. Shumlak, A Discontinuous Galerkin Method for Ideal Two-Fluid Plasma Equations, Communications in Computational Physics 9 (2) (2011) 240–268. URL https://doi.org/10.4208/cicp.250509.210610a
- 965 [53] J. Loverich, U. Shumlak, Nonlinear full two-fluid study of m=0 sausage instabilities in an axisymmetric Z pinch, Physics of Plasmas 13 (2006) 082310. URL https://doi.org/10.1063/1.2220009
  - [54] A. Hakim, U. Shumlak, Two-fluid physics and field-reversed configurations, Physics of Plasmas 14 (2007) 055911.URL https://doi.org/10.1063/1.2742570
- 970 [55] I. A. M. Datta, D. W. Crews, U. Shumlak, Electromagnetic extension of the Dory-Guest-Harris instability as a benchmark for Vlasov-Maxwell continuum kinetic simulations of magnetized plasmas (in press), Physics of Plasmas 28 (7) (2021). URL https://doi.org/10.1063/5.0057230
- [56] S. Miller, Modeling collisional processes in plasmas using discontinuous numerical methods, Ph.D. thesis, University of Washington, Seattle, WA (2016).

  URL https://www.aa.washington.edu/sites/aa/files/faculty/shumlak/research/cpdlab/docs/miller\_
  - sean\_dissertation.pdf [57] R. J. Leveque, Finite Volume Methods for Hyperbolic Problems, Cambridge University Press, 2002.
  - [58] V. V. Rusanov, The calculation of the interaction of non-stationary shock waves and obstacles, USSR Computational Mathematics and Mathematical Physics 1 (2) (1962) 304–320.

    URL https://doi.org/10.1016/0041-5553(62)90062-9
    - [59] A. Harten, P. D. Lax, B. V. Leer, On Upstream Differencing and Godunov-Type Schemes for Hyperbolic Conservation Laws, SIAM Review 25 (1) (1983) 35–61. URL https://doi.org/10.1137/1025002
- 985 [60] P. L. Roe, Approximate Riemann solvers, parameter vectors, and difference schemes, Journal of Computational Physics 43 (2) (1981) 357–372. URL https://doi.org/10.1016/0021-9991(81)90128-5
  - [61] S.-Q. Han, W.-P. Song, Z.-H. Han, An improved WENO method based on Gauss-kriging reconstruction with an optimized hyper-parameter, Journal of Computational Physics 422 (2020) 109742. URL https://doi.org/10.1016/j.jcp.2020.109742
  - [62] T. Buffard, T. Gallouët, J.-M. Hérard, A sequel to a rough Godunov scheme: application to real gases, Computers & Fluids 29 (7) (2000) 813–847. URL https://doi.org/10.1016/S0045-7930(99)00026-2
- [63] X. Cai, X. Zhang, J. Qiu, Positivity-Preserving High Order Finite Volume HWENO Schemes for Compressible Euler Equations, Journal of Scientific Computing 68 (2016) 464–483.

- ${\rm URL\ https://doi.org/10.1007/s10915\text{-}015\text{-}0147\text{-}8}$
- [64] P. Cagas, A. Hakim, J. Juno, B. Srinivasan, Continuum kinetic and multi-fluid simulations of classical sheaths, Physics of Plasmas 24 (022118) (2017) 1–11. URL http://doi.org/10.1063/1.4976544
- 1000 [65] S. Robertson, Sheaths in laboratory and space plasmas, Plasma Physics and Controlled Fusion 55 (9) (2013) 093001.
  - URL https://doi.org/10.1088/0741-3335/55/9/093001
  - [66] T. H. Stix, Waves In Plasmas, API, New York, New York, 1992.
  - [67] A. B. Mikhailovskii, Electromagnetic Instabilities in an Inhomogenous Plasma, Vol. 1, IOP Publishing Ltd, New York, New York, 1992.
  - [68] G. V. Vogman, J. H. Hammer, W. A. Farmer, Customizable two-species kinetic equilibria for nonuniform low-beta plasmas, Physics of Plasmas 26 (2019) 042119. URL https://doi.org/10.1063/1.5089465
  - [69] H. S. M. Coxeter, Regular Polytopes, Methuen & Co. Ltd., London, UK, 1948.